Large eddy simulation of a row of impinging jets with upstream crossflow using the lattice Boltzmann method

Minh Nguyen, Jean-François Boussuge, Pierre Sagaut, Juan-Carlos Larroya-Huguet

Large eddy simulation of a row of impinging jets with upstream crossflow using the lattice Boltzmann method

Minh Nguyen[a,b,*], Jean-François Boussuge[b], Pierre Sagaut[c], Juan-Carlos Larroya-Huguet[a]

[a] Safran Aircraft Engines, Rond Point René Ravaud, Moissy-Cramayel 77550, France
[b] CERFACS, 42 Avenue Gaspard Coriolis, Toulouse 31057, France
[c] Aix Marseille Univ, CNRS, Centrale Marseille, M2P2 UMR 7340, 38 rue Joliot-Curie, Marseille 13451, France

ARTICLE INFO

Article history:
Received 9 November 2022
Revised 3 April 2023
Accepted 30 April 2023
Available online 15 May 2023

Keywords:
Lattice boltzmann method
Multi-jet impingement
Large eddy simulation
Compressible impinging jet
Row of jets
Crossflow

ABSTRACT

Large eddy simulations of a row of seven jets emerging from a perforated pipe and impinging on a flat heated plate were carried out using a compressible hybrid thermal lattice Boltzmann solver. The average Reynolds number of the emerging jets was 5 000, with an exit-to-plate distance of 3 jet diameters. Two levels of upstream crossflow were simulated: one with weak cross flow, with a velocity ratio of ≈ 9.7, and one with strong cross flow, with a velocity ratio of ≈ 2. The flow field and heat transfer statistics were validated against experimental PIV and infrared thermography data from a recent study, showing good agreement. The effect of varying the Mach number on the wall heat transfer was subsequently tested. It was found that an increased Mach number lead to an increased value of the Nusselt number near the stagnation points.

1. Introduction

Impinging jet configurations, which can be used to produce high rates of convective heat transfer, are found in a wide variety of industrial applications. These include the cooling of machine components such as turbine blades or electronic devices, the drying of food products, and the heating of airplane wings to prevent ice formation.

A single axisymmetric impinging jet is typically divided into a free jet region, where the jet is not affected by the impacted surface, a stagnation region, where the jet is slowed down by the wall and deflected outward, and a wall jet region, where the jet largely flows parallel to the wall. At low nozzle-to-plate distance, this test case is known for exhibiting two peaks in the radial Nusselt number distribution: a primary peak near the stagnation point, and a secondary peak further downstream, in the wall jet region. This configuration has been the subject of extensive experimental [1–5] and numerical [6–11] research, along with numerous literature reviews [12–14], many of which seek to explain the existence of the two peaks. As a result, despite the existence of many possible parameters (nozzle geometry, Reynolds number, Mach number, confinement, plate distance), the aerothermal behavior of this test case, and its variation based on changes to the aforementioned parameters, are fairly well understood. However, for single impinging jets, the level of heat transfer can decline rapidly with distance from the stagnation region, and as a result, single jet impingement is typically effective in cooling only a small area. In order to efficiently cool a surface, multi-jet configurations are often used.

The use of more than one jet substantially increases the complexity of the flow phenomena, and adds additional parameters whose effects are less well understood. The configuration is no longer axisymmetric and becomes fully three-dimensional. The jets can interact with one another both before and after they impact the plate. The jets can be arranged as a single row along one axis, or as an array of multiple inline or staggered rows of jets [15], or following a 2 or 3-dimensional form [16]. If the jet nozzles are supplied by a fluid flow whose direction is not strictly normal to the hole of the nozzles, the jets have a condition of upstream cross flow, which leads to a distortion in the shape of the jet. This adds additional complexity to the flow phenomena, and introduces an additional parameter (the degree of upstream crossflow). Likewise, the jets can also exit into a domain where an existing flow parallel to the impacted surface is present, leading to a condition of downstream crossflow.

Multiple jet impingement has also been investigated experimentally and numerically [17–19]. The greater physical complexity and wider number of parameters involved in multijet configurations with crossflow make the use of computational fluid dynamics (CFD) attractive as a means of predicting the most optimal configuration.

* Corresponding author.
E-mail address: nguyen@cerfacs.fr (M. Nguyen).

Nomenclature

τ_{update}	Update period for dynamic mass flow condition [s]
μ	Dynamic viscosity [kgm^{-1}s^{-1}]
$K_{cbc,in}$	characteristic boundary condition inlet relaxation coefficient [s^{-1}]
$K_{dyn,out}$	dynamic pressure outlet relaxation coefficient [s^{-1}]
$\mathcal{T}_{\alpha\beta}$	Viscous stress tensor [kgm^{-1}s^{-1}]
ρ	Density [kgm^{-3}]
γ	Ratio of specific heats [ ]
x, y, z	Cartesian coordinates [m]
u_x, u_y, u_z	Cartesian velocity [ms^{-1}]
u_τ	Friction velocity [ms^{-1}]
R_s	Specific gas constant [Jkg^{-1}K^{-1}]
p	Pressure [Pa]
c	Speed of sound $= \sqrt{\gamma R_s T}$ [ms^{-1}]
Ma_j	Jet Mach Number $= \frac{U_j^{eff}}{c}$ [ ]
s	Entropy [Jkg^{-1}K^{-1}]
Multi-Jet Variables	
λ	Thermal conductivity [Wm^{-1}K^{-1}]
D_j	Jet hole diameter [m]
D_p	Pipe inner diameter [m]
Δj	Hole spacing [m]
H	Injection-to-plate distance [ms^{-1}]
A_j	Hole cross-sectional area $\pi D_j^2/4$ [s^2]
A_p	Pipe cross-sectional area $\pi D_p^2/4$ [s^2]
VR	Velocity ratio [ ]
U_j^{nom}	Nominal jet bulk speed [ms^{-1}]
U_j^{eff}	Effective jet bulk speed $\approx 1.4U_j^{nom}$ [ms^{-1}]
U_p	Pipe bulk speed [ms^{-1}]
$(\rho U)_{j,avg}$	Average jet bulk momentum magnitude [kgs^{-1}m^{-1}]
$(\rho U)_p$	Pipe bulk momentum magnitude [kgs^{-1}m^{-1}]
$\dot{m}$	Mass flow rate [kgs^{-1}]
Re_j	Jet Reynolds number $= \frac{(\rho U)_{j,avg} D_j}{\mu}$ [ ]
q_w	Wall heat flux [Wm^{-2}]
T_p	Pipe inflow temperature [K]
T_j	Jet temperature [K]
T_w	Wall temperature [K]
T_{ref}	Reference temperature for heat transfer [K]
h	Heat transfer coefficient $= \frac{q_w}{T_w - T_{ref}}$ [Wm^{-1}K^{-1}]
Nu	Nusselt number $= \frac{hD_j}{\lambda_{ref}}$ [ ]
λ_{ref}	Thermal conductivity for calculation of the Nusselt number [Wm^{-1}K^{-1}]
τ_{impact}	Nominal jet flow-through time $= \frac{3D_j}{U_j^{nom}}$ [s]
LBM Variables	
$\mathcal{R}$	Hybrid recursive regularized operator [ ]
$\overline{\psi}_i^*$	Forcing corrective term [ ]
$c_{i\alpha}^*$	Discrete velocity [ ]
c_s^*	Lattice constant [ ]
f_i^*	Distribution function [ ]
f_i^{eq*}	Equilibrium distribution function [ ]
f_i^{neq*}	Off-equilibrium distribution function [ ]
$\overline{\tau}^*$	Relaxation time [ ]
Operators	
RMS	Root-mean-square
$\langle\ \rangle$	Time averaging
$^+$	Wall units

Reynolds-Averaged Navier-Stokes (RANS) approaches remain the most commonly used family of methods for turbulent flow simulations of industrial relevance. However, these approaches have difficulty in reliably predicting the flow field and heat transfer of multi-jet impingement configurations [13]. Although $k-\omega$ SST and $\overline{v^2}-f$ based models have been recommended for this family of test cases, many RANS multi-jet studies show significant discrepancies in the heat transfer distribution [20,21]. As a result, higher fidelity-simulations, typically those involving Large Eddy Simulation (LES) approaches, are highly attractive for these configurations, particularly when precise results are required.

There are relatively few LES studies of impinging multi-jet configurations in the literature. Draksler et al. [16] performed a study of an array of jets arranged in a hexagonal shape, with no upstream crossflow. Their simulation produced good agreement with the experimental configuration. Hossain et al. [22] simulated a single row of jets exiting into a narrow channel, and were likewise able to accurately predict the flow field and heat transfer. Otero-Pérez et al. [23] performed LES of a multi-jet configuration with downstream crossflow, whereas Ahmimache (2022b) [24] carried out an LES of a row of impinging jets with upstream crossflow. To the authors' knowledge, these are the only LES that have been performed on multi-jet configurations, with the last one being the only one performed on an impinging jet test case with strong upstream crossflow. It is likely that LES studies for these configurations are limited by their high computational cost.

Due to the high cost of traditional Navier-Stokes based LES, the Lattice Boltzmann Method (LBM) has emerged as an alternative means of performing LES. The principal element of the LBM is the collide-and-stream algorithm, which has low rates of dissipation and dispersion [25] while typically only making use of immediate neighbors, rendering it efficient for massively parallel computing [26,27]. The use of Cartesian meshes can be paired with octree refinement, significantly accelerating mesh generation. LBM approaches have been tested on industrial configurations and have produced good results at a lower computational cost compared to Navier-Stokes methods [28].

Although LBM approaches have typically been limited to isothermal, weakly compressible flows, new LBM models have made it possible to simulate thermal compressible flows [29–35]. They combine a Lattice Boltzmann algorithm for the resolution of the mass and momentum equations, coupled with a finite difference/finite volume scheme for the resolution of the energy scheme. This approach has been tested on the classic round impinging jet test case with a Reynolds number of 23 000 and a nozzle-to-plate spacing of two diameters [36], yielding very good agreement with previous experimental and numerical investigations of this configuration. However, the method has remained untested for more complex aerothermal jet simulations.

Recently, Ahmimache et al. (2022a) [37] performed an in-depth study of a configuration based on a single row of impinging jets with upstream crossflow. The test case is composed of a perforated pipe whose holes produce jets that impact upon a heated flat surface. It is a test case that is meant to represent a simplified geometry of an Active Clearance Control (ACC) sytem, meant to cool a turbine casing in order to induce a contraction in its size and reduce the blade tip gap. They examined the effects of different nozzle-to-plate spacings, upstream crossflow intensities, jet Reynolds numbers, and nozzle-to-nozzle spacings, and performed an in-depth study on their effects on the flow field statistics and heat transfer properties. This configuration thus possesses ample experimental data that can be used to validate a numerical simulation approach. One of the main objectives of this work is thus to validate the hybrid LBM approach for complex aerothermal flows by performing LBM-Large Eddy Simulations on the perforated pipe

test case of Ahmimache et al. (2022a) [37] for two levels of upstream crossflow.

Furthermore, although the database of Ahmimache et al. (2022a) [37] is based on low speed incompressible flows, ACC systems can involve jets of higher velocity [24,38], where compressibility effects are not negligible. Compressibility effects on multi-impinging jet configurations are not well characterized. The experiments of Goodro et al. [39–41] on multiple arrays of jets indicate that at constant Reynolds number, an increase of the Mach number yields increased heat transfer. By contrast, the RANS study of Ben Ahmed [42] shows a decrease in heat transfer with increasing Mach number. In the present study, the hybrid LBM solver is fully compressible, and these effects can be investigated. This is done here on one of the configurations, via the Pressure Gradient Scaling (PGS) [43] approach, where the value of the specific gas constant R_s in the ideal gas relation $p = \rho R_s T$ is adjusted. Three Mach numbers are investigated: $Ma \approx 0.08$ (corresponding to the true physical conditions of the experiment of Ahmimache et al. (2022a) [37]), $Ma \approx 0.30$, and $Ma \approx 0.50$.

This paper is organized in the following sections. In Section 2, the hybrid LBM solver used in this study is briefly detailed, along with an additional mass flow rate condition used to ensure the correct conditions are being simulated. Section 3 describes the numerical setup of the test case: the geometry, configurations, boundary conditions, fluid properties, meshes, and simulation strategy are detailed. In Section 4, first, the results of the simulations at low Mach number are validated against the experimental data. Next, the effects of compressibilty on the Nusselt number distribution are investigated.

2. Overview of the thermal LBM approach

2.1. Hybrid thermal compressible LBM

Within this section, the variables written in non-dimensional form are denoted using the subscript *. This is done using $\rho_0, \Delta x, T_0, \Delta t = \frac{\Delta x c_s^*}{\sqrt{R_s T_0}}$, where $c_s^* = \sqrt{1/3}$ is the non-dimensional lattice constant. The simulations in this work are carried out using the Lattice Boltzmann solver ProLB [44], which has recently been adapted for carrying out complex thermal flows. The model uses an improved density-based thermal equilibrium distribution function [34] with isotropy correction [45], together with a hybrid regularized recursive (HRR) collision operator, coupled with an entropy equation solved with finite difference/finite volume scheme, using the MUSCL approach [32,34,46]. The collide-and-stream algorithm, in non-dimensional form, is as follows:

$$f_i^*(x_\alpha^* + c_{i\alpha}^*, t^* + 1) = f_i^{eq*}(x_\alpha^*, t) + (1 - \frac{1}{\tau^*})\mathcal{R}(f_i^{neq*}) + \frac{1}{2}\psi_i^*(x_\alpha^*, t^*), \tag{1}$$

where f_i^* is the particle distribution function, with the subscript i representing the index of the discrete lattice velocities $c_{i\alpha}^*$. Here, the D3Q19 lattice is used. f_i^{eq*} is the equilibrium distribution function, $\mathcal{R}(f_i^{neq*})$ is the off-equilibrium distribution reconstructed using the HRR collision operator (see [29–34,46]), $\overline{\tau}^*$ represents the nondimensional relaxation time $\overline{\tau}^* = \mu^*/(\rho^* c_s^2) + \frac{1}{2}$, and ψ_i^* is a forcing term used to correct discretization errors produced by this LBM approach.

The equilibrium distribution function is written as:

$$f_i^{eq*} = \omega_i \rho^* (f_i^{eq,\ (0)*} + f_i^{eq,\ (1)*} + f_i^{eq,\ (2)*} + f_i^{eq,\ (3)*}). \tag{2}$$

ω_i are the standard weights for the D3Q19 lattice. The term at order 0 is defined as:

$$f_i^{eq,\ (0)*} = 1 + d_i, \text{where } d_i = \begin{cases} \frac{\omega_0 - 1}{\omega_0}(T^* - 1), & \boldsymbol{c}_i^* = (0,0,0) \\ T^* - 1, & \text{else.} \end{cases} \tag{3}$$

The term at order 1 is:

$$f_i^{eq,\ (1)*} = \frac{c_{i\alpha}^*}{c_s^{*2}} u_\alpha^*. \tag{4}$$

The term at order 2 is based on the isotropy correction of Bauer et al. [45]. It leads to the correct calculation of certain fourth order moments and is:

$$f_i^{eq,\ (2)*} = \begin{cases} -u_\alpha^* u_\alpha^*, & \boldsymbol{c}_i^* = (0,0,0) \\ -3u_\alpha^* u_\alpha^* + 6(c_{i\alpha}^* u_\alpha^*)^2, & \boldsymbol{c}_i^* \in \{(\pm 1, 0, 0), \\ & (0, \pm 1, 0), (0, 0, \pm 1)\} \\ -\frac{3}{2} c_{i\alpha}^{*2} u_\alpha^{*2} + \frac{9}{2}(c_{i\alpha}^* u_\alpha^*)^2, & \text{else.} \end{cases} \tag{5}$$

Lastly, the term at order 3 is equal to:

$$\begin{aligned} f_i^{eq,\ (3)*} = \tfrac{1}{6c_s^{2*}} \Big[& 3(\mathcal{H}_{ixxy}^{(3)*} + \mathcal{H}_{iyzz}^{(3)*})(u_x^* u_x^* u_y^* + u_y^* u_z^* u_z^*) + \\ & (\mathcal{H}_{ixxy}^{(3)*} - \mathcal{H}_{iyzz}^{(3)*})(u_x^* u_x^* u_y^* - u_y^* u_z^* u_z^*) + \\ & 3(\mathcal{H}_{ixzz}^{(3)*} + \mathcal{H}_{ixyy}^{(3)*})(u_x^* u_z^* u_z^* + u_x^* u_y^* u_y^*) + \\ & (\mathcal{H}_{ixzz}^{(3)*} - \mathcal{H}_{ixyy}^{(3)*})(u_x^* u_z^* u_z^* - u_x^* u_y^* u_y^*) + \\ & 3(\mathcal{H}_{iyyz}^{(3)*} + \mathcal{H}_{ixxz}^{(3)*})(u_y^* u_y^* u_z^* + u_x^* u_x^* u_z^*) + \\ & (\mathcal{H}_{iyyz}^{(3)*} - \mathcal{H}_{ixxz}^{(3)*})(u_y^* u_y^* u_z^* - u_x^* u_x^* u_z^*) \Big]. \end{aligned} \tag{6}$$

where $H_{i\alpha\beta\gamma}^{(3)*}$ are the LBM Hermite polynomials at order three:

$$\mathcal{H}_{i\alpha\beta\gamma}^{(3)*} = c_{i\alpha}^* c_{i\beta}^* c_{i\gamma}^* - c_s^{*2}\left(c_{i\alpha}^* \delta_{\beta\gamma} + c_{i\beta}^* \delta_{\gamma\alpha} + c_{i\gamma}^* \delta_{\alpha\beta},\right). \tag{7}$$

It can be seen, that in contrast to the classic isothermal LBM, variable temperature T^* is present within the equilibrium distribution function, leading to an expression for pressure equal to $p^* = \rho^* c_s^{*2} T^*$ in non-dimensional terms, or $p = \rho R_s T$ in dimensional terms. On standard lattices, the present equilibrium distribution function leads to errors in the viscous stress tensor (including the Mach error present in standard LBM approaches), which are corrected via the term ψ_i^*:

$$\psi_i^* = \omega_i \frac{\mathcal{H}_{i\alpha\beta}^{(2)*}}{2c_s^{*4}} \Psi_{\alpha\beta}^*, \tag{8}$$

defined such that

$$\begin{aligned} \Psi_{\alpha_\beta}^* = & c_s^{*2} u_\alpha^* \tfrac{\partial(\rho^*(1-T^*))}{\partial x_\beta^*} + c_s^{*2} u_\beta^* \tfrac{\partial(\rho^*(1-T^*))}{\partial x_\alpha^*} + \\ & \tfrac{2}{3}\delta_{\alpha\beta}\rho^* c_s^{*2} \tfrac{\partial u_\gamma^*}{\partial x_\gamma^*} - \delta_{\alpha\beta} c_s^{*2} \tfrac{\partial \rho^*(1-T^*)}{\partial t^*} + \tfrac{\partial Err_{\alpha\beta\gamma}^*}{\partial x_\gamma^*}. \end{aligned} \tag{9}$$

where $\frac{\partial Err_{\alpha\beta\gamma}^*}{\partial x_\gamma^*}$ is the term derived from the inability of standard lattices to recover third order moments:

$$\frac{\partial Err_{\alpha\beta\gamma}^*}{\partial x_\gamma^*} = -\begin{bmatrix} \frac{\partial \rho^* u_x^* u_x^* u_x^*}{\partial x^*} & \frac{\partial \rho^* u_x^* u_y^* u_z^*}{\partial z^*} & \frac{\partial \rho^* u_x^* u_y^* u_z^*}{\partial y^*} \\ \frac{\partial \rho u_x^* u_y^* u_z^*}{\partial z^*} & \frac{\partial \rho^* u_y^* u_y^* u_y^*}{\partial y^*} & \frac{\partial \rho^* u_x^* u_y^* u_z^*}{\partial x^*} \\ \frac{\partial \rho^* u_x^* u_y^* u_z^*}{\partial y^*} & \frac{\partial \rho^* u_x^* u_y^* u_z^*}{\partial z^*} & \frac{\partial \rho^* u_z^* u_z^* u_z^*}{\partial z^*} \end{bmatrix} \tag{10}$$

When coupled with an entropy equation, the equivalent macroscopic equations are the compressible Navier-Stokes equations, with the energy equation based on entropy s:

$$\frac{\partial \rho}{\partial t} + \frac{\partial \rho u_\alpha}{\partial x_\alpha} = 0, \tag{11}$$

$$\frac{\partial \rho u_\alpha}{\partial t} + \frac{\partial(\rho u_\alpha u_\beta + p\delta_{\alpha\beta})}{\partial x_\beta} = \frac{\partial}{\partial x_\beta}\mathcal{T}_{\alpha\beta}. \tag{12}$$

$$\frac{\partial s}{\partial t} + u_\alpha \frac{\partial s}{\partial x_\alpha} = \frac{1}{\rho T}\frac{\partial}{\partial x_\alpha}(-q_\alpha) + \frac{1}{\rho T}\mathcal{T}_{\alpha\beta}\frac{\partial u_\alpha}{\partial x_\beta} \tag{13}$$

Where $\mathcal{T}_{\alpha\beta}$ is the viscous stress tensor:

$$\mathcal{T}_{\alpha\beta} = \mu\left(\frac{\partial u_\alpha}{\partial x_\beta} + \frac{\partial u_\beta}{\partial x_\alpha} - \frac{2}{3}\frac{\partial u_\gamma}{\partial x_\gamma}\right). \tag{14}$$

and q_α is the heat flux:

$$q_\alpha = \lambda \frac{\partial T}{\partial x_\alpha}. \tag{15}$$

A full reconstruction approach is used for the boundaries, and the direct coupling (DC) algorithm of Astoul et al. [47], adapted for thermal flows, is used for grid transitions. The subgrid scale terms are modeled using the shear-improved Smagorinsky model of Lévêque et al. [48]. This model is based on the Smagorinsky model, but reduces the value of turbulent viscosity in zones of mean shear such as boundary layers and shear layers.

2.2. Mass flow rate boundary conditions

In the present work, the only deviation from the model used in [36] is the use of mass flow rate boundary conditions. These are required in order to ensure that the correct flow configuration is being solved. Navier-Stokes Characteristic Boundary conditions (NSCBC) are used for in and outflow conditions, using the Local One Dimensional Inviscid (LODI) [49] approximation, and adapted for LBM approaches [50]. From Lodato et al. [51,52], the outgoing wave $\mathcal{L}_5$ corresponding to normal velocity u_n for non-reflecting turbulent inflow condition, if transverse terms are neglected, can be rewritten as:

$$\mathcal{L}_5 = \rho c\left(K_{cbc,in}\left(u_n - u_n^t\right) - \frac{\partial u_n^t}{\partial t}\right), \tag{16}$$

where $K_{cbc,in}$ is a relaxation coefficient (in Hz), and u_n^t is the target normal velocity. The time derivative $\frac{\partial u_n^t}{\partial t}$ term is used if inflow perturbations (turbulence injection) are used. For a mass flow rate condition, $\mathcal{L}_5$ is simply modified such that:

$$\mathcal{L}_5 = \rho c\left(\frac{K_{cbc,in}}{\rho}\left((\rho u)_n - (\rho u)_n^t\right) - \frac{\partial u_n^t}{\partial t}\right). \tag{17}$$

In the case where there are multiple outlets, and therefore multiple mass flow rates to be specified, an additional boundary condition is required in order to ensure the correct distribution of flow through the separate outlets. For this case, the approach proposed by Odier et al. [53] is used. The pressure imposed on the dynamic outlet is updated every τ_{update} periods of time such that:

$$p_{n+1} = p_n + K_{dyn,\ out}(\langle\dot{m}\rangle - \dot{m}^t) \tag{18}$$

where the subscript n represents the given period, $K_{dyn,\ out}$ is another relaxation coefficient, $\langle\dot{m}\rangle$ is the mass flow rate through the outlet averaged over τ_{update}, and $\dot{m}^t$ is the target mass flow rate. Thus, at every period n of duration τ_{update}, the actual mass flow rate is evaluated and compared to the target mass flow rate. If, for example, the mass flow rate is too low, at the next period $n+1$, the imposed pressure is changed such that $p_{n+1} < p_n$. This imposed pressure is used as a target for the classical NSCBC pressure outlet of [49–51].

3. Setup

3.1. Geometry and configurations

The configuration is presented in Fig. 1a and is composed of a perforated pipe embedded into a rectangular cuboid domain. It is the same geometry as the one studied experimentally by Ahmimache et al. (2022a) [37]. The seven holes along the pipe are circular and uniform, and are of diameter D_j. They are directly normal to a heated flat plate. Fluid is supplied to the pipe at mass flow rate $\dot{m}_1$. When the fluid reaches the holes, it forms jets which impinge upon the heated plate. The amount of flow that goes through the pipe holes is denoted $\dot{m}_2$, and this flow is allowed to leave the domain through a larger hole. At the opposite side of the pipe inlet, either a solid wall is placed, (henceforth called case 1, or C1), or a mass flow $\dot{m}_3$ is allowed to leave the pipe domain (henceforth called case 2, or C2). For C1, since the end of the pipe is blocked off, all of the inflow entering the pipe leaves through the pipe holes, and thus $\dot{m}_1 = \dot{m}_2$. For C2, $\dot{m}_1 = \dot{m}_2 + \dot{m}_3$.

Table 1
Summary of the physical properties of the cases.

	Case 1	Case 2
Re_j	5 000	5 000
$\Delta j/D_j$	2.25	2.25
H/D_j	3	3
VR	9.7	2
$\dot{m}_1$ [kgs^{-1}]	0.002	0.0097
$\dot{m}_2$ [kgs^{-1}]	0.002	0.002
$\dot{m}_3$ [kgs^{-1}]	0	0.0077
Ma_j	$\approx 0.08, 0.30, 0.50$	≈ 0.08

A detailed view of the XZ and YZ planes (respectively at $y = 0$ and $x = 0$) of the computational domain is shown in Fig. 1b. The dimensions are written in terms of the hole diameter $D_j = 4$ mm. The pipe has an inner diameter $D_p = 8.2D_j = 32.8$ mm, and an outer diameter of $10D_j = 40$ mm. The holes are spaced evenly with a distance $\Delta j = 2.25D_j$. The inset in Fig. 1b shows the two possible configurations C1 and C2, showing a blocked and open pipe exit respectively. The nozzle-to-plate spacing is $H/D_j = 3$. The heated plate is a rectangle of size $[L_x \times L_y] = [20D_j \times 15D_j]$ and its center is placed directly above the central hole. The origin of the domain is placed at the center of the exit of the central hole.

One of the means of quantifying the two cases is by means of the speed or velocity ratio VR, which is the ratio of the bulk speed or bulk momentum magnitude of the jets relative to that of the pipe. This parameter is defined as:

$$VR = \frac{(\rho U)_{j,avg}}{(\rho U)_p} \tag{19}$$

where $(\rho U)_{j,avg}$ is the average bulk momentum magnitude of the jets, $(\rho U)_p$ is the bulk momentum magnitude through the pipe, A_p is the cross-sectional area of the pipe, and A_j is the cross-sectional area of each of the seven holes.

The two cases are summarized in Table 1. They correspond to two of the test cases investigated by Ahmimache et al. (2022a) [37]. For case 1, since the pipe exit is blocked off, $\dot{m}_1 = \dot{m}_2$. Based strictly on conservation of mass and the area ratio $\frac{A_p}{7A_j}$, the ratio between the pipe and jet bulk momenta is 9.606, compared to a nominal value of $VR = 9.7$ used to describe the experimental test case. This difference is attributed to uncertainties in the experimental equipment [37]. As the characteristic jet speed is ≈ 9.7 times greater than the speed of the pipe flow, crossflow effects are relatively weak for this configuration. By contrast, for case 2, the characteristic jet speed is only ≈ 2.0 times greater than the speed of the pipe flow, and as a result, crossflow effects are significantly stronger than for case 1.

Ma_j in the table corresponds to the approximate Mach number of the jets exiting from the holes. For both cases, the mass flow rate through the holes $\dot{m}_2 = 2\text{gs}^{-1}$, corresponds to a jet bulk momentum magnitude $(\rho U)_{b,j} = 22.73642\text{kgm}^{-1}\text{s}^{-1}$. With an approximate density of $\approx 1.1762\text{kgm}^{-3}$, this corresponds to a nominal bulk speed of $U_j^{nom} = 19.33\text{ms}^{-1}$. However, the *vena contracta* effect reduces the cross-sectional area of the jet, and in reality, the jets exit at $\approx 27 - 30$m/s. The approximate effective velocity

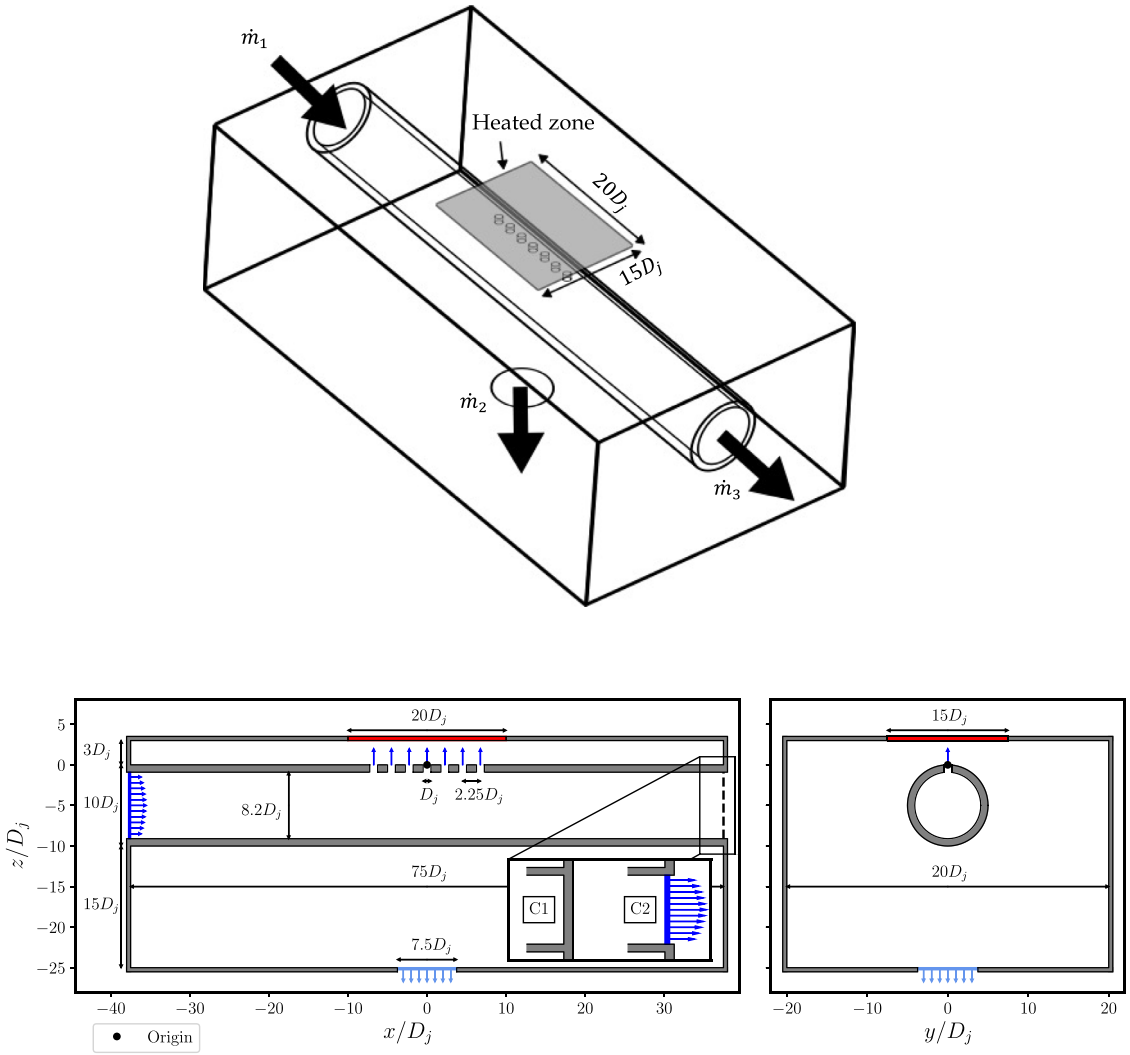

Fig. 1. Diagrams of the simulated geometry and the two possible cases.

$U_j^{eff} = 1.4U_j^{nom}$ is used to calculate the Mach number used to denote the test cases. $Ma_j \approx 0.08$ represents the real physical conditions studied in the experiment, whereas $Ma_j \approx 0.30$ and $Ma_j \approx 0.50$ correspond to additional studies performed here, using the PGS approach.

3.2. Fluid properties and boundary conditions

The working fluid has a specific gas constant of $R_s = 287.15\text{Jkg}^{-1}\text{K}^{-1}$ for the configuration corresponding to the real experiments ($Ma_j \approx 0.08$). For the investigation of higher Mach numbers, $R_s = 20.42\text{Jkg}^{-1}\text{K}^{-1}$ for the $Ma \approx 0.3$ case, and $R_s = 7.35\text{Jkg}^{-1}\text{K}^{-1}$ for the $Ma \approx 0.5$ case. The dynamic viscosity is set to $\mu_{ref} = 1.82 \times 10^{-5}\text{kgm}^{-1}\text{s}^{-1}$, with variation based on Sutherland's law. The Sutherland reference temperature is set to $T = 300K$, (which is the temperature imposed at the pipe inlet), for the $Ma \approx 0.08$ and $Ma_j \approx 0.30$ cases. For the $Ma_j \approx 0.50$ case, the acceleration of the fluid through the jet holes leads to a loss in static temperature, leading to $T_j \approx 287K$. In order to maintain the same jet Reynolds number, the Sutherland reference temperature is set to $287K$ for this case.

For C1, the mass inflow of $\dot{m}_1 = 2\text{gs}^{-1}$ corresponds to a pipe bulk momentum magnitude $(\rho U)_p = 2.367\text{kgm}^{-1}\text{s}^{-1}$, yielding a pipe Reynolds number $Re_p = 4266$. A power law profile for the specific momentum is prescribed at the inlet using the NSCBC condition described in 2.2. The profile is defined such that

$$(\rho U)_x(r) = (\rho U)_{cl}\left(1 - \frac{r}{R}\right)^{1/n}, \tag{20}$$

with the centerline velocity $(\rho U)_{x,cl} = 1.31(\rho U)_p$ and $n = 5.15$. The centerline coefficient is taken from the DNS of El Khoury at $Re_b = 5\ 300$ [54], with n chosen to ensure that the integral of the momentum profile corresponds to the correct mass flow. Homogeneous Isotropic Turbulence (HIT), based on the approach of Béchara et al. and Bailly and Juvé [55,56] is injected across the inlet plane. A static temperature of $T_p = 300K$ was imposed at the inlet. The outlet pressure corresponding to $\dot{m}_2$ is set to $p_{\dot{m}_2} = 101325\text{Pa}$. All of the walls except for the central plate are adiabatic no-slip walls. For the central plate, first an initial simulation with an adiabatic no-slip wall is run in order to obtain T_{aw}, after which a heat flux condition with $q_w = 4000\text{Wm}^{-2}$ is imposed (for the cases involving PGS, $q_w = 284.4\text{Wm}^{-2}$ for $Ma \approx 0.30$ and 102.4Wm^{-2} for $Ma \approx 0.50$ to maintain dimensional consistency). Each combination of the configuration and mesh thus has an adiabatic run and a heat flux run.

For C2, this configuration adds an additional degree of complication to the numerical simulation, as two mass flow conditions must be controlled in order to attain the correct Reynolds numbers (and hence crossflow intensities). The mass inflow of $\dot{m}_1 = 9.7\text{gs}^{-1}$

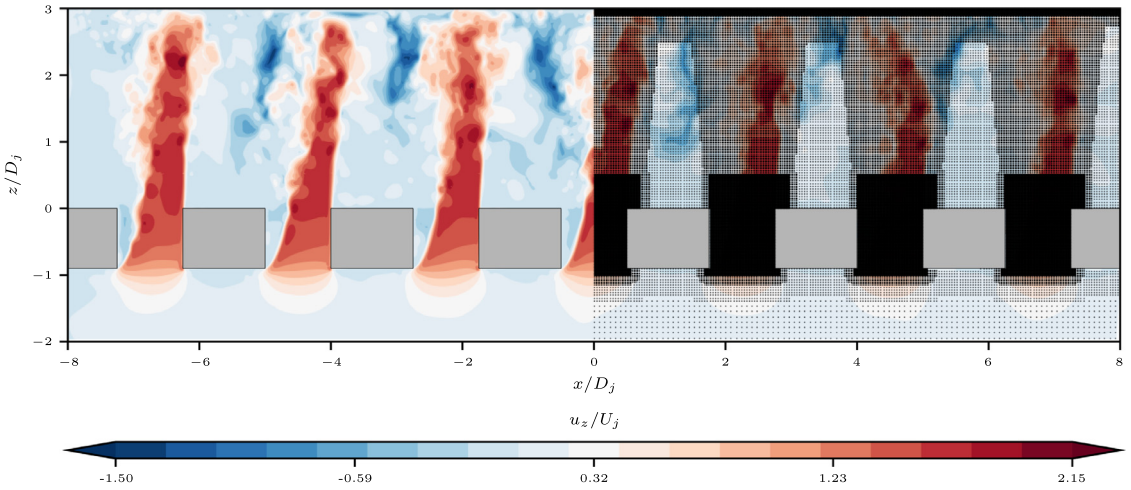

Fig. 2. Zoomed X-Z cross-section of instantaneous non-dimensional axial velocity for Case 2, along with the grid points of Mesh 2.

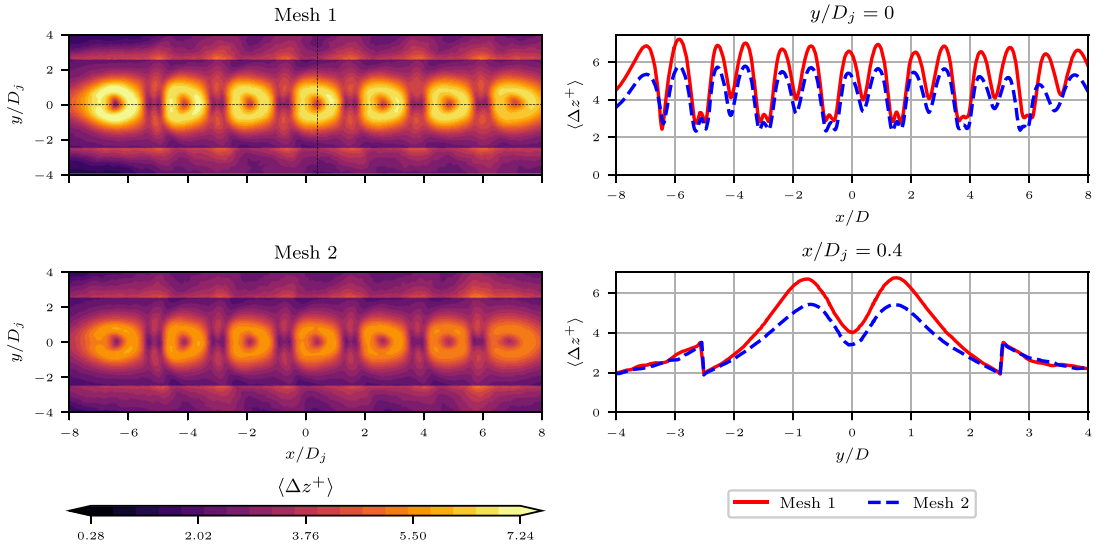

Fig. 3. Non-dimensional mesh element size Δz^+ on the impacted plate, for Case 1, $Ma_j \approx 0.08$.

corresponds to a pipe bulk momentum magnitude $(\rho U)_{b,p} = 11.47979\text{kgm}^{-1}\text{s}^{-1}$, yielding a pipe Reynolds number $Re_p = 20\,464$. As in C1, a power law profile with HIT is imposed with the same static temperature condition, this time with $(\rho U)_{cl} = 1.262(\rho U)_{b,p}$ and $n = 6.05$. The outlet pressure corresponding to $\dot{m}_2$ is likewise set to $p_{\dot{m}_2} = 101325\text{Pa}$. However, for the pipe outlet, a dynamic pressure condition (described in Section 2.2) is imposed so that $\dot{m}_3 = 7.7\text{gs}^{-1}$. The initial guess for the pressure was set to $p_{\dot{m}_2,\ n=0} = 101925\text{Pa}$. The wall conditions are identical to the ones of C1.

In order to alter the Mach number of the jets, three values of the gas constant R_s are chosen. Given a jet temperature of $T_j \approx 300K$, the Mach number is approximately $0.08, 0.30, 0.50$ for the values of $R_s = 287.15, 20.42, 7.35$.

3.3. Meshing strategy

When using octree mesh structures, the zones where different mesh sizes are used are referred to as Resolution Domains (RD). Here, RD1 refers to zones where the finest grid spacing is used. Grid spacing in RD2 is 2× greater than the spacing in RD1, and in RD3 it is 4× greater, and so on. Nodes in RD2 are updated only half as often as nodes in RD1 (meaning that the time step for RD2 is double that of RD1). As a result, the notion of "equivalent" fine nodes can be introduced. An RD2 node is counted as having the cost of 1/2 that of an RD1 node, and an RD3 node is counted as 1/4, and so on.

An instantaneous snapshot of the axial velocity and grid points can be seen in Fig. 2, showing the mesh topology on the right hand side. In all cases, RD1 points are reserved for the jet holes and the points near the impingement surface. For C1, the Reynolds number in the pipe is low ≈ 4 300, and therefore, RD4 is used near the pipe walls, with RD5 used in the bulk flow of the pipe. For C2, because the pipe Reynolds number is higher, RD3 is used near the pipe walls, with RD4 used in the bulk flow.

Table 2 provides a quantitative description of the grids for Case 1. Case 2 has similar grid properties, but results in about ≈ 15% more CPU time for the same physical time, due to the extra points placed in the central pipe due to the higher Reynolds number. The meshes are identical for the PGS cases with $Ma \approx 0.30$ and $Ma \approx 0.50$. However, due to the increased time step relative to the flow-through-time, these cases require 3 and 4 times fewer time steps than the baseline case, respectively.

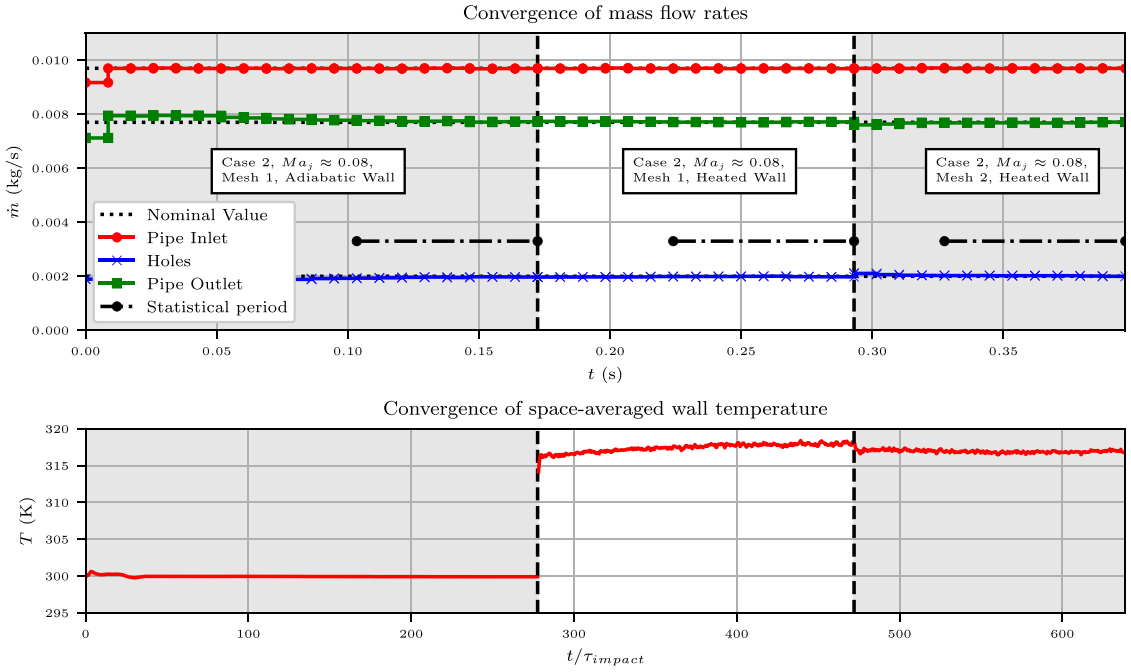

Fig. 4. Evolution of the mass flow rate and spatially averaged wall temperature over time for the different simulations used for Case 2, $Ma_j \approx 0.08$.

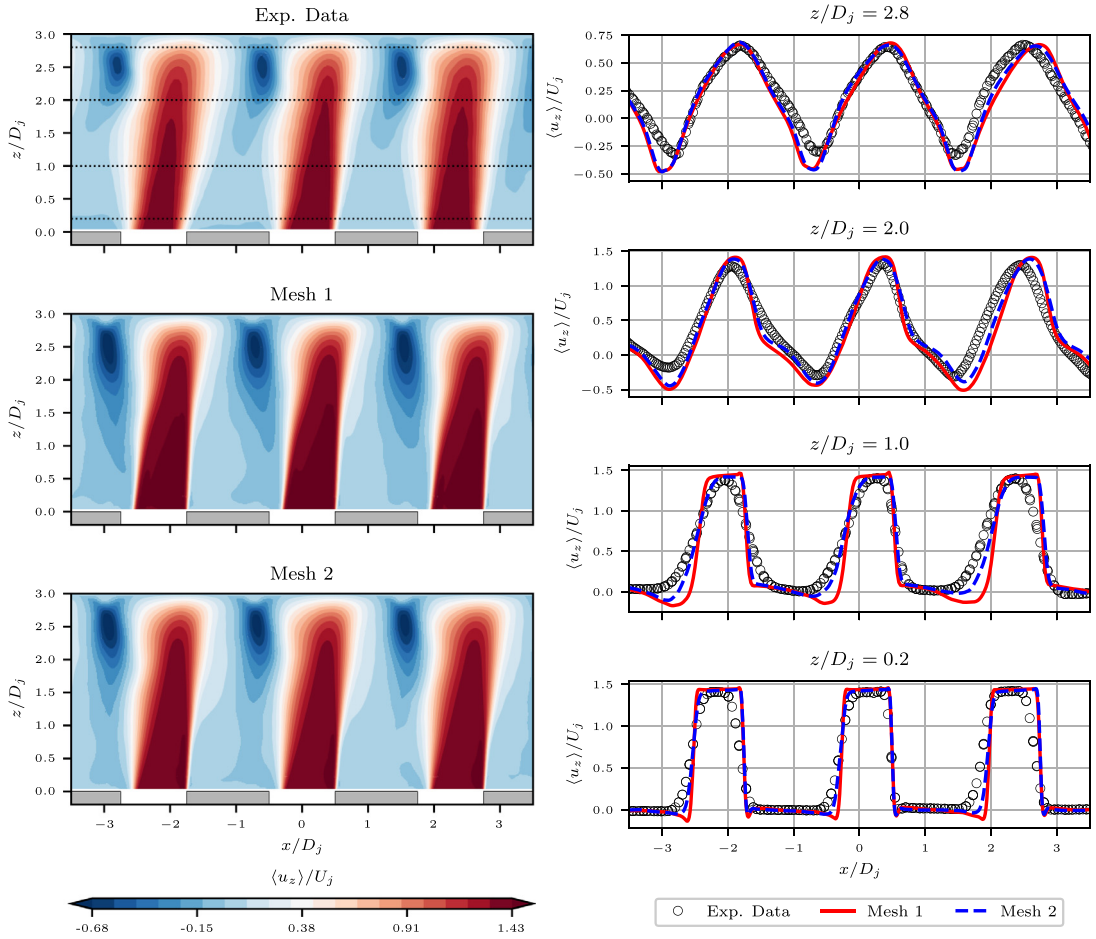

Fig. 5. Comparison of $\langle u_z \rangle$ for a cut in the XZ plane, $y = 0$, for Case 1, $Ma_j \approx 0.08$. The dotted lines in the upper left contour represent the z locations of the 1D profiles.

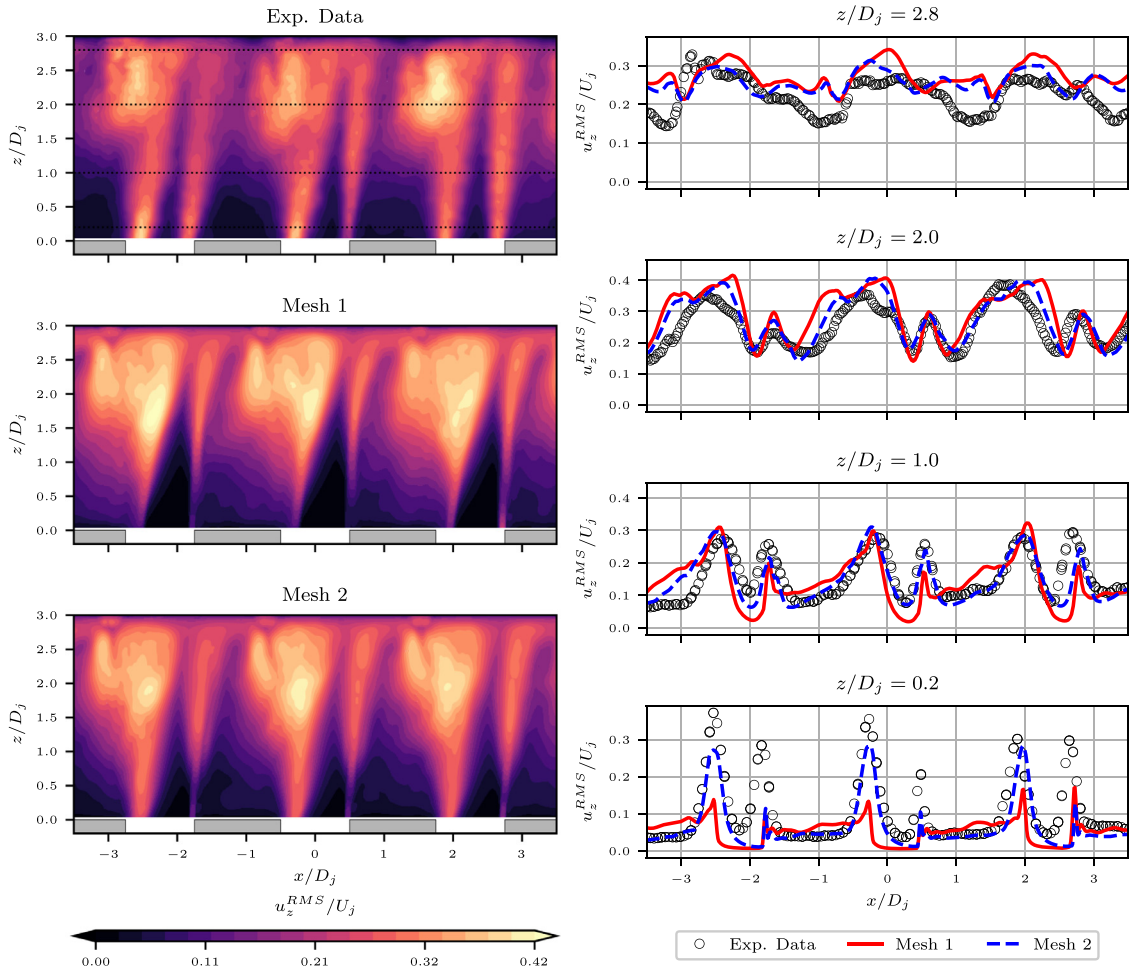

Fig. 6. Comparison of u_z^{RMS} for a cut in the XZ plane, $y = 0$, for Case 1, $Ma_j \approx 0.08$. The dotted lines in the upper left contour represent the z locations of the 1D profiles.

Table 2
Summary of the properties of the different meshes. C1M1 = Configuration 1 Mesh 1, C1M2 = Configuration 1 Mesh 2.

	C1M1	C1M2
$\Delta(x,y,z)_{RD1}/D_{jet}$	0.0125	0.01
$\Delta(x,y,z)_{\max}/D_{jet}$	0.4	0.32
Total Points (M)	21.68	40.48
Eq. Fine Points (M)	13.31	25.12
Δt (s)	$8.9785 \cdot 10^{-8}$	$7.1828 \cdot 10^{-8}$
$N_{\Delta t}$ for τ_{impact}	6914.26	8642.82
$N_{\Delta t}$ for τ_{stats}	768 000	960 000
CPU time for τ_{stats}	9164.97	19672.49

A visualization of the near-wall distance Δz^+ is shown in Fig. 3. The maximal values ($\approx 7, 5.9$ for meshes 1 and 2, respectively) are higher than the typically recommended of ≈ 2 value for typical LES wall boundary layers [57]. However, satisfactory flow field results using LBM solvers have been found for larger values [58,59]. Furthermore, the near-wall flow physics of an impinging jet differ significantly from that of a typical boundary layer, with good heat transfer results being reported for LES with wall-normal distances superior to 2 [9,36]. For impinging jets, it has previously been reported that high levels of grid stretching near the wall leads to poor results [6,7]. Since the mesh is entirely composed of cubes, the stream and spanwise grid point distance is equivalent to the wall-normal distance, producing excellent resolution in these directions.

3.4. Simulation strategy and convergence

The flow field and heat transfer statistics are all based on a statistical time of $\tau_{stat} \approx 111\tau_{impact}$, where $\tau_{impact} = 3\frac{D_j}{U_j^{nom}}$ is the flow-through time from the holes to the wall, based on the nominal bulk speed $U_j^{nom} = 19.33\text{ms}^{-1}$. In order to make sure that the effects of compressibility are properly accounted for, each configuration is simulated with both an adiabatic and a heated wall condition at the plate. For the sake of consistency, this is performed across all Mach numbers, even if it will be shown in Section 4.3 that this is unnecessary for $Ma_j \approx 0.08$. The simulations are run sequentially, with a typical order as follows:

1. C1M1, adiabatic wall,
2. C1M1, imposed heat flux,
3. C1M2, imposed heat flux,

with the proceeding simulation being initialized with the field based on the time step of the previous simulation. The statistics are taken after a transient period that is determined using the temporal convergence of the mass flow rate and the space-averaged wall temperature.

Fig. 4 shows the convergence of the mass flow rate and space-averaged wall temperature for Case 2, $Ma \approx 0.08$. It can be seen that after a period of adaptation, the outlet condition at the end of the pipe is able to adjust its pressure such that the correct distribution of fluid is achieved between the holes

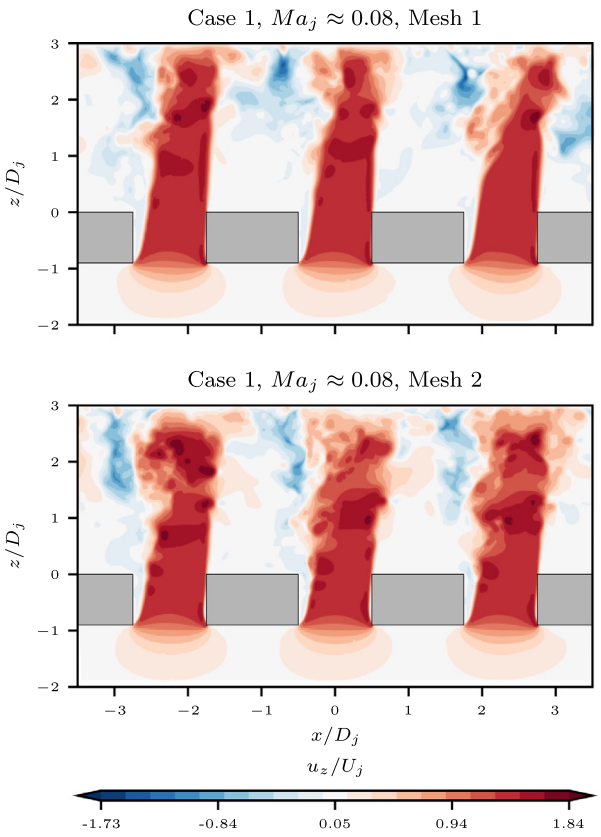

Fig. 7. Comparison of instantaneous u_z for the two meshes at a cut in the *XZ* plane, $y = 0$, for Case 1, $Ma_j \approx 0.08$.

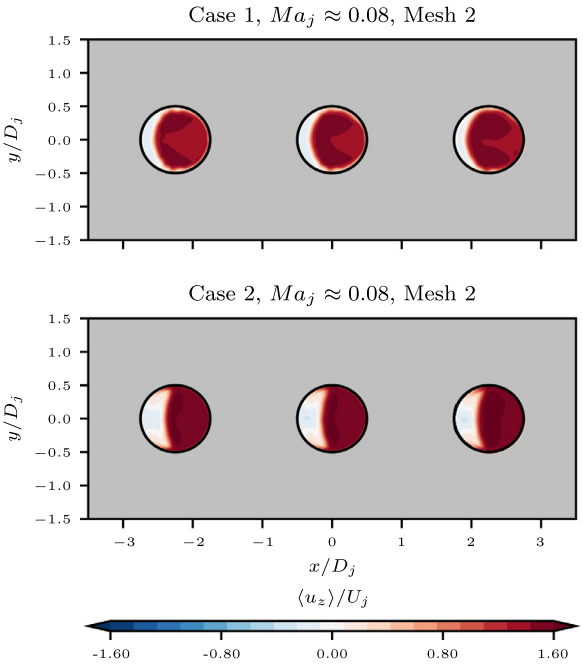

Fig. 8. Comparison of $\langle u_z \rangle$ for the two cases, $Ma_j \approx 0.08$, at a cut in the *XY* plane, $z/D_j = -0.1$, for Mesh 2.

and the pipe exit. In all of the cases studied here, the mass flow rates evaluated over the statistical period are within 1% of the target values. Since the corresponding experimental study reports a mass flow uncertainty of 2% [37], this is considered satisfactory.

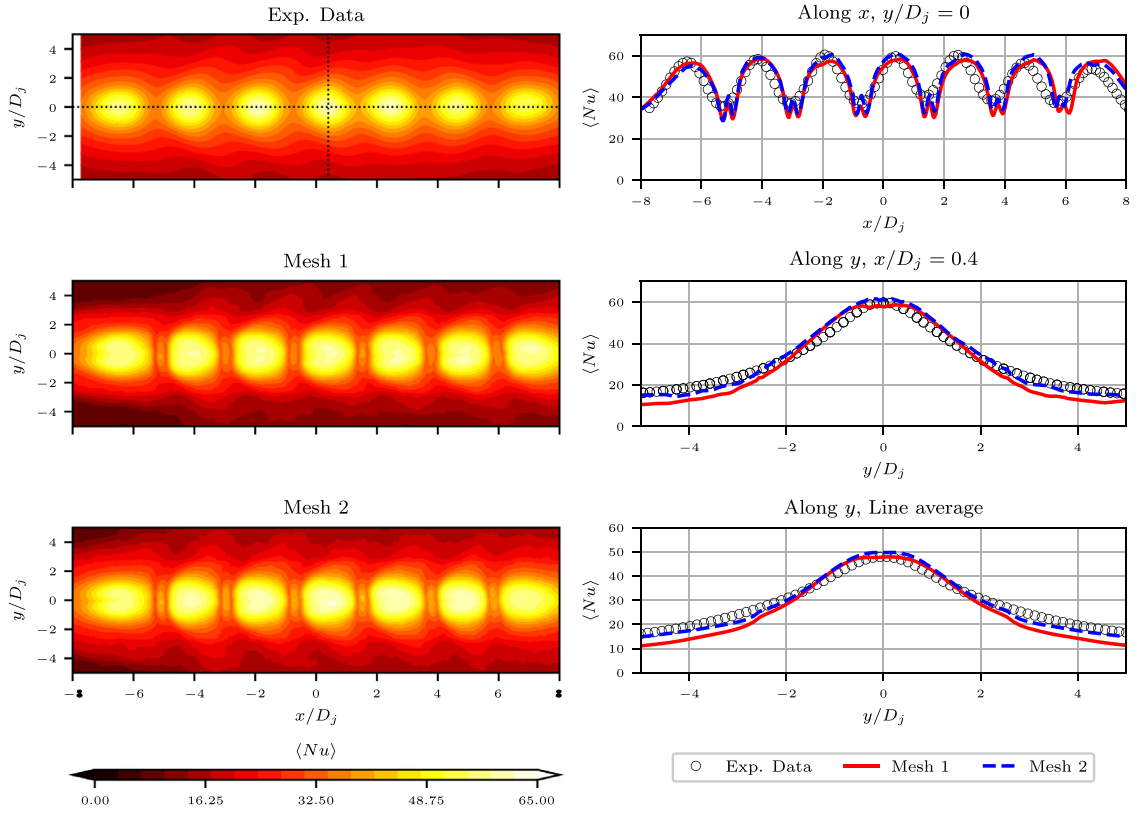

Fig. 9. Comparison of the Nusselt number for the two meshes, for Case 1, $Ma_j \approx 0.08$. The dotted lines in the upper left contour represent the locations of the cuts for the profiles along *x* and *y*.

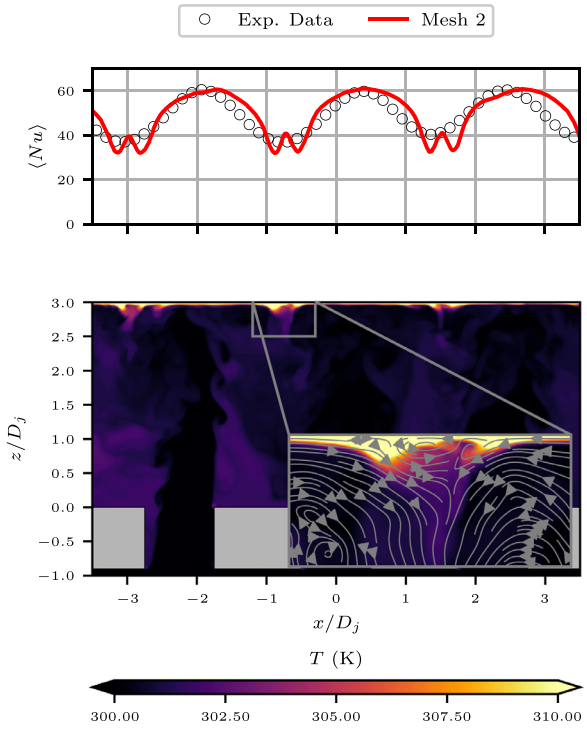

Fig. 10. Mean Nusselt number (top) and instantaneous aerothermal field near the wall (bottom), with zoom at one of the locations of a secondary peak, for Case 1, Mesh 2, $Ma_j \approx 0.08$.

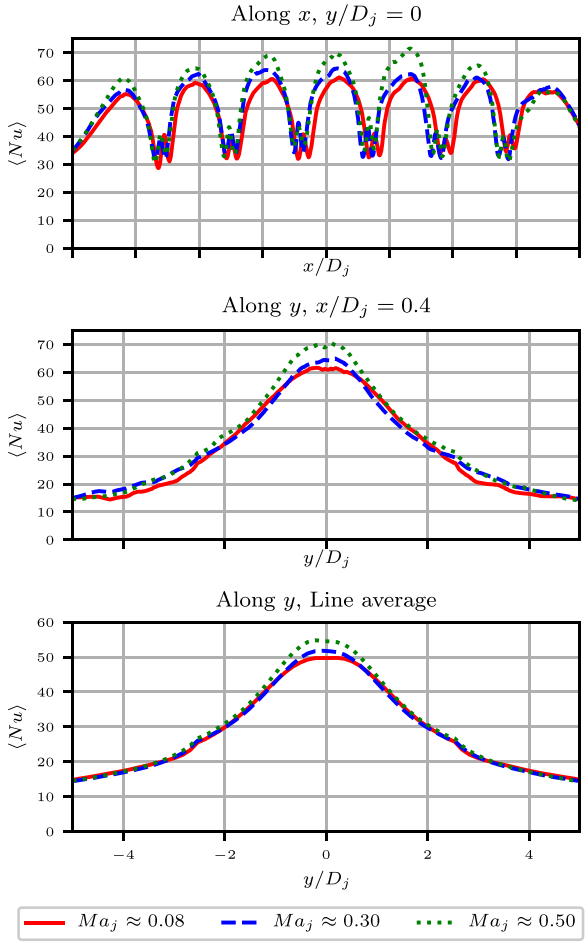

Fig. 11. Comparison of the Nusselt number for the three Mach numbers, for Case 1, Mesh 2.

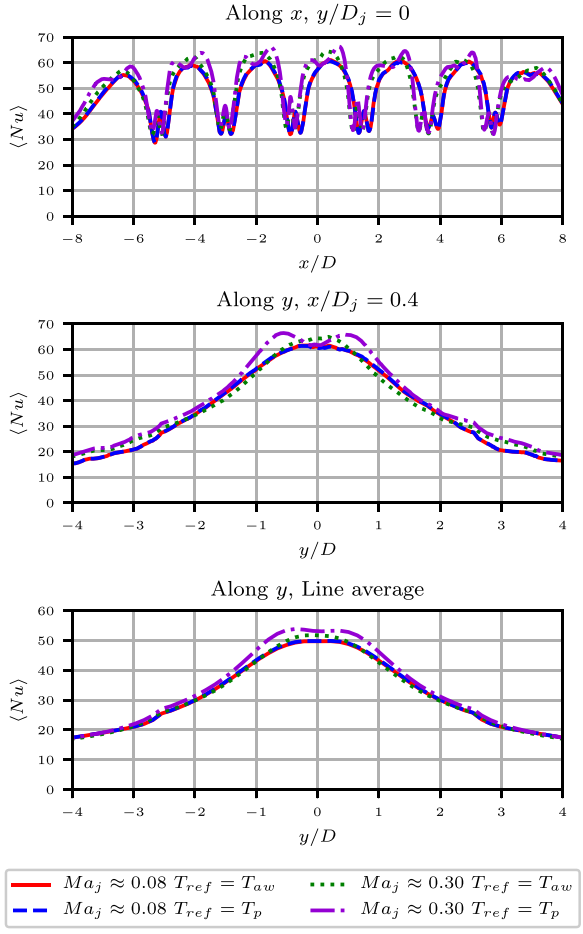

Fig. 12. Comparison of the Nusselt number for two Mach numbers, for Case 1, Mesh 2, using different normalization temperatures.

4. Results and discussion

4.1. Validation of the flow field

Fig. 5 shows a cut in the XZ plane at $y = 0$ of the mean axial velocity at the three central holes, along with the 1D velocity profiles along x on lines at $z/D_j = 0.2, 1.0, 2.0, 2.8$, for Case 1. Fig. 6 shows the same profiles, but for the velocity fluctuations.

The qualitative 2D velocity profile shows good agreement between the experiments and the LBM-LES. However, it can be clearly seen that the LBM-LES results have "thicker" jet cores that persist longer in the axial direction than those seen in the experimental data. Examining the 1D velocity profile at $z/D_j = 0.2$, both LBM-LES meshes produce roughly the same results, with slightly flatter profiles than the experimental results. By contrast, at $x/D_j = 1.0$, Mesh 2 produces better agreement, as the jet core has been reduced in width, indicating that the finer mesh better captures the development of the jet. Closer to the wall, at $z/D_j = 2.0$ and $z/D_j = 2.8$, all both meshes produce results that are in good agreement with the experimental data, although the LES shows a more powerful fountain zone, with stronger levels of negative axial velocity.

The discrepancies between the numerical simulations and the experimental data in the 2D fields are greater for the velocity fluctuations than for the mean velocity. Notably, it can be seen that the shear layers show weaker fluctuations near the holes. This contrast is particularly visible in the right shear layers, which, for both meshes, show little fluctuations until around

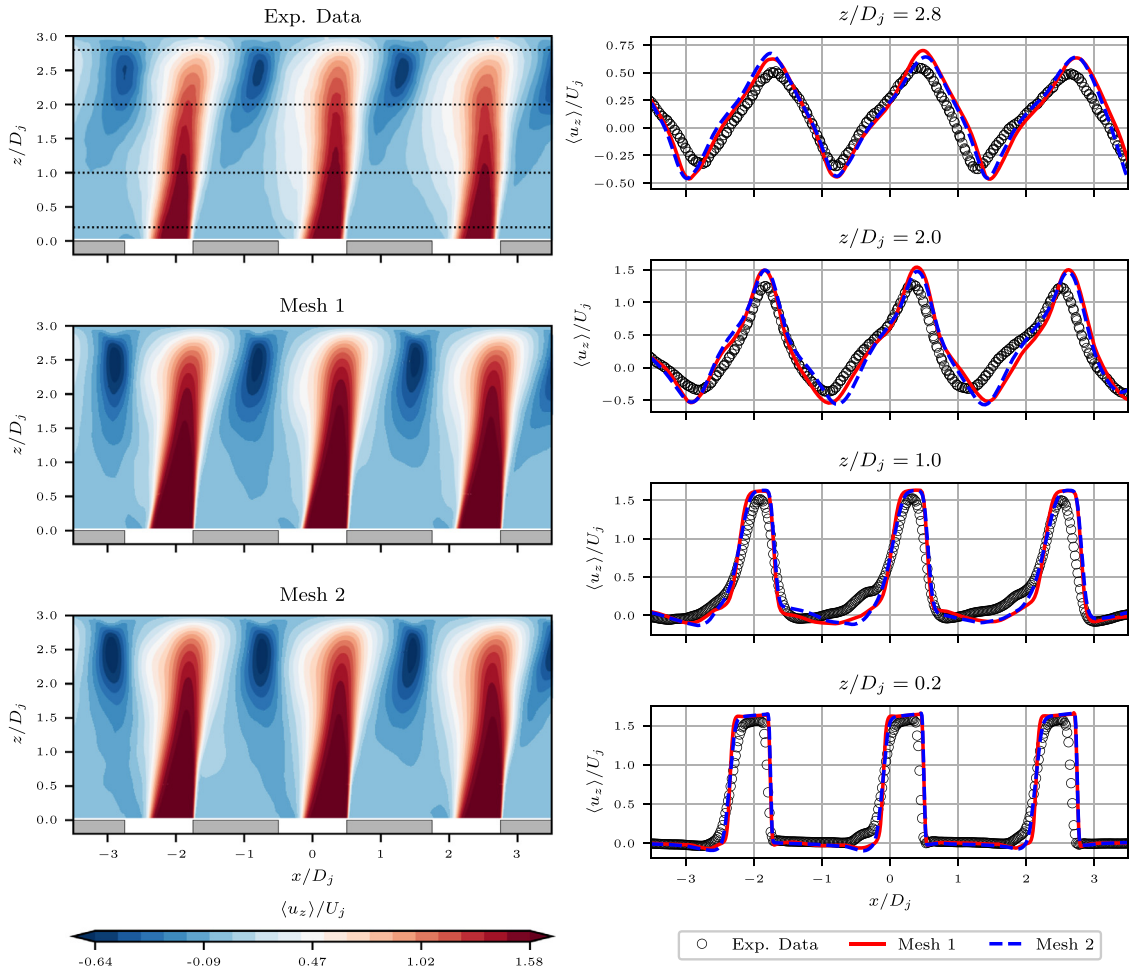

Fig. 13. Comparison of $\langle u_z \rangle$ for a cut in the XZ plane, $y = 0$, for Case 2, $Ma_j \approx 0.08$. The dotted lines in the upper left contour represent the z locations of the 1D profiles.

$z/D_j \approx 0.5$. For the left shear layer, the finer mesh is better able to capture the Kelvin-Helmholtz instability and the transition to turbulence.

The same profiles as Figs. 5 and 6, but for Case 2 instead of Case 1, can be found at Figs. 13 and 14, in Appendix A.1. The conclusions are by and large, the same as for Case 1, although the jets are significantly thinner for Case 2 than for Case 1, as the much stronger upstream crossflow leads to a greater degree of jet deformation, and produces thinner shear layers.

The destabilization of the shear layer can be seen in the instantaneous profiles of axial velocity for Case 1 for both meshes in Fig. 7. The breakdown of the roughly irrotational potential core occurs via a "pinching" action induced by the generated vortical structures [60]. It can be seen that the finer mesh leads to an earlier breakdown of the laminar shear layer, as was seen in Figs. 5 and 6. This test case involves the acceleration of the fluid through the holes, producing jets where the jet shear layers undergo transition via the Kelvin-Helmholtz instability with a $Re \approx 5\ 000$, a process that represents a particular challenge. The Reynolds number is sufficiently low such that the transition to turbulence is not immediate in the numerical simulations. The simulation must use sufficient points, and have a sufficiently non-dissipative numerical scheme, in order to capture this phenomenon. However, it can be seen in Figs. 5 and 6 that further downstream, at stations $z/D_j = 2.0$ and $z/D_j = 2.8$, the two meshes produce very similar results, suggesting that the delayed transition to turbulence exhibited by the first mesh does not lead to serious discrepancies in the flow field near the wall.

Fig. 8 shows the mean velocity profiles for cases 1 and 2, for mesh 2, at a distance of $0.1D_j$ upstream of the nozzles, inside the pipe perforations. It can be seen that both profiles are not axisymmetric, with a reduction of the effective area of the jet seen on the left, which was described in the experimental study of Fénot et al. (2016) [61]. The degree of non-axisymmetry is greater for Case 2 than for Case 1, and the smaller effective area of the jets of Case 2 means that the gradients are sharper, meaning even more points are required to effectively capture the shear layer behavior.

The three-dimensional nature of this test case presents additional difficulty compared to typical long pipe jets. For long pipe jets, mesh refinement can be placed in the pipe boundary layer, which can be extended into the free jet shear layer: the user knows *a priori* where the zones of strong shear are, and can therefore mesh accordingly. This is typical in long pipe jet LES studies [6,7,10,36]. In the present test case, the three-dimensional nature of this flow renders the placement of additional refinement zones in the jet shear layer significantly more complicated, thus leading to the wholesale refinement in the holes, as seen in Fig. 2. The presence of "wasted" points in this current simulation (of which there are more for Case 2 than for Case 1) renders the future use of adaptive mesh refinement techniques attractive.

4.2. Validation of the wall heat transfer

The Nusselt number is defined as:

$$Nu = \frac{hD_j}{\lambda_{ref}}, \tag{21}$$

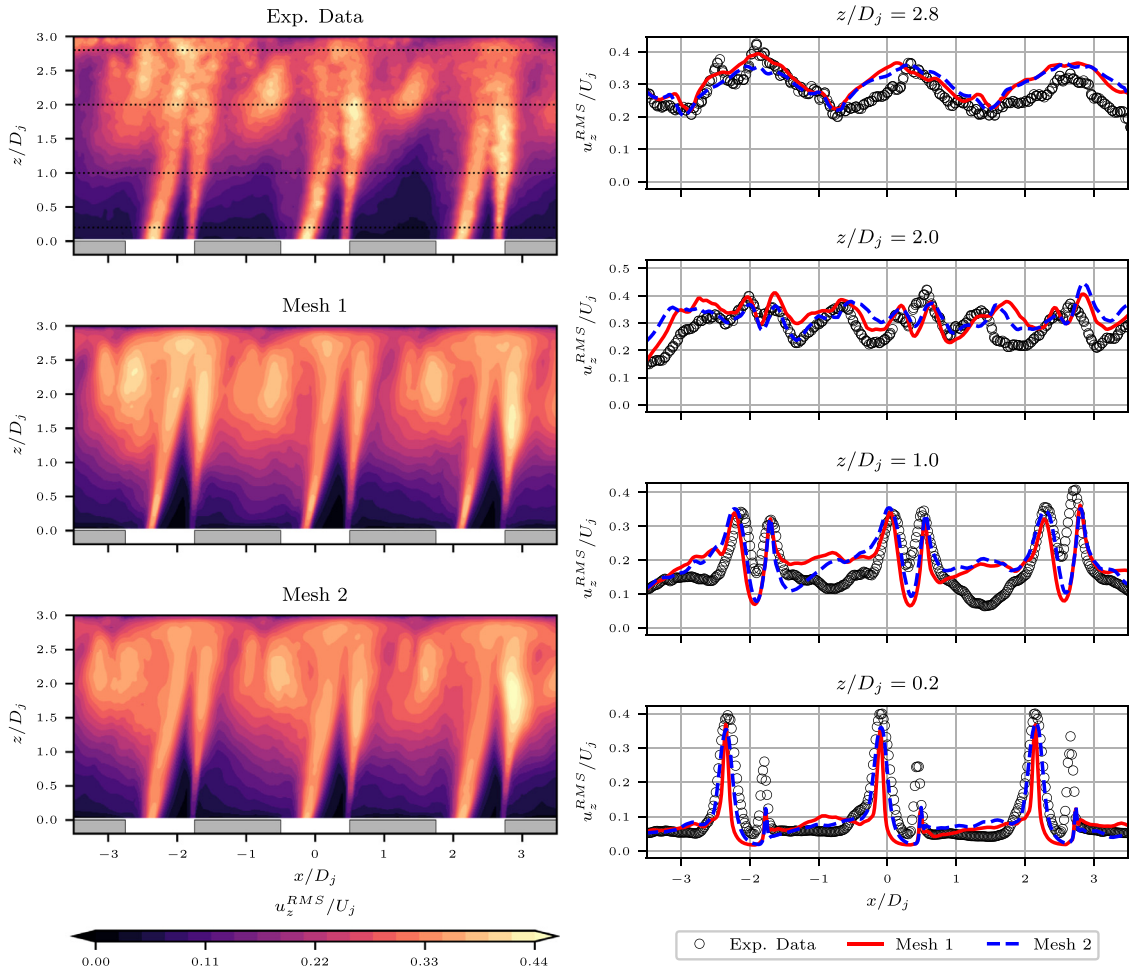

Fig. 14. Comparison of u_z^{RMS} for a cut in the XZ plane, $y = 0$, for Case 2, $Ma_j \approx 0.08$. The dotted lines in the upper left contour represent the z locations of the 1D profiles.

where λ_{ref} is a reference thermal conductivity, and h is the heat transfer coefficient, defined as:

$$h = \frac{q_w}{T_w - T_{ref}}, \tag{22}$$

where q_w is the wall heat transfer (imposed as a boundary condition):

$$q_w = \left(\lambda(T = T_w) + \lambda_{sgs}\right) \frac{\partial T}{\partial n}|_w. \tag{23}$$

where $\lambda(T = T_w)$ is the thermal conductivity that varies according to Sutherland's law, λ_{sgs} is the subgrid scale thermal conductivity, and $\frac{\partial T}{\partial n}|_w$ is the temperature gradient at the heated wall.

The choice of T_{ref} can play a crucial role in the profile of the Nusselt number [62]. If the jet is incompressible, and the jet temperature is equivalent to the ambient temperature, then $T_{ref} = T_j$ can be chosen. However, if either of those two criteria are not respected, then the proper choice is $T_{ref} = T_{aw}$, with T_{aw} the wall temperature for an equivalent jet test case, but with an adiabatic wall instead of a heated one. In this section of this work, $T_{ref} = T_{aw}$ is used to calculate h, and $\lambda_{ref} = \lambda(T = T_j)$ for the calculation of Nu. The effects of the choice of T_{ref} are discussed in Section 4.3.

The first column of Fig. 9 shows the time-averaged 2D Nusselt number profile at the impacted plate for Case 1, comparing the results of the experiments with that of the LBM-LES. The second column compares the profile along x along the row centerline ($y/D_j = 0$), along y at the location of the central stagnation point ($x/D_j = 0.4$), and the line-averaged y profile between $-5.25 \leq x/D_j \leq 6.05$ (which covers the five central holes).

For the distribution along x, it can be seen that both meshes recover the Nusselt number distribution with a high degree of precision, in particular at the stagnation points. At this location, the difference between the two meshes is relatively minor. For the three jets on the right, the stagnation points are shifted very slightly to the right, but otherwise show good agreement.

Small intermediate peaks of the Nusselt number can be seen in between stagnation points, which are not present in the experimental results. Within the present simulation results, these secondary peaks are a result of the collision of adjacent wall jets and the formation of the fountain effect, as seen in Fig. 10. "below" the fountain effect, a secondary vortex is formed, leading to a recirculation bubble that brings cool fluid in contact with the wall. In contrast to the secondary peak in the Nusselt number found for single axisymmetric jets, these peaks are attested at any given instant of the simulation. The secondary vortices are described by Carcasci [63], and were attested in the PIV study of Ichikawa et al. [64]. The presence of secondary peaks at the location of two adjacent wall jets is also attested by the infrared camera study of Wae-Hayee, et al. [65]. The LES results of Draksler et al. [16] attest similar secondary peaks. It is possible that the IR camera results of Ahmimache et al. [37] did not possess sufficient resolution to detect these secondary peaks.

The profile along y at $x/D_j = 0.4$ shows similarly good agreement. Mesh 1 shows a fairly significant underestimation of the Nusselt number further away from the stagnation point, whereas Mesh 2 follows the experimental data quite well. The line-averaged data, which allows for the heat transfer of the five central jets to

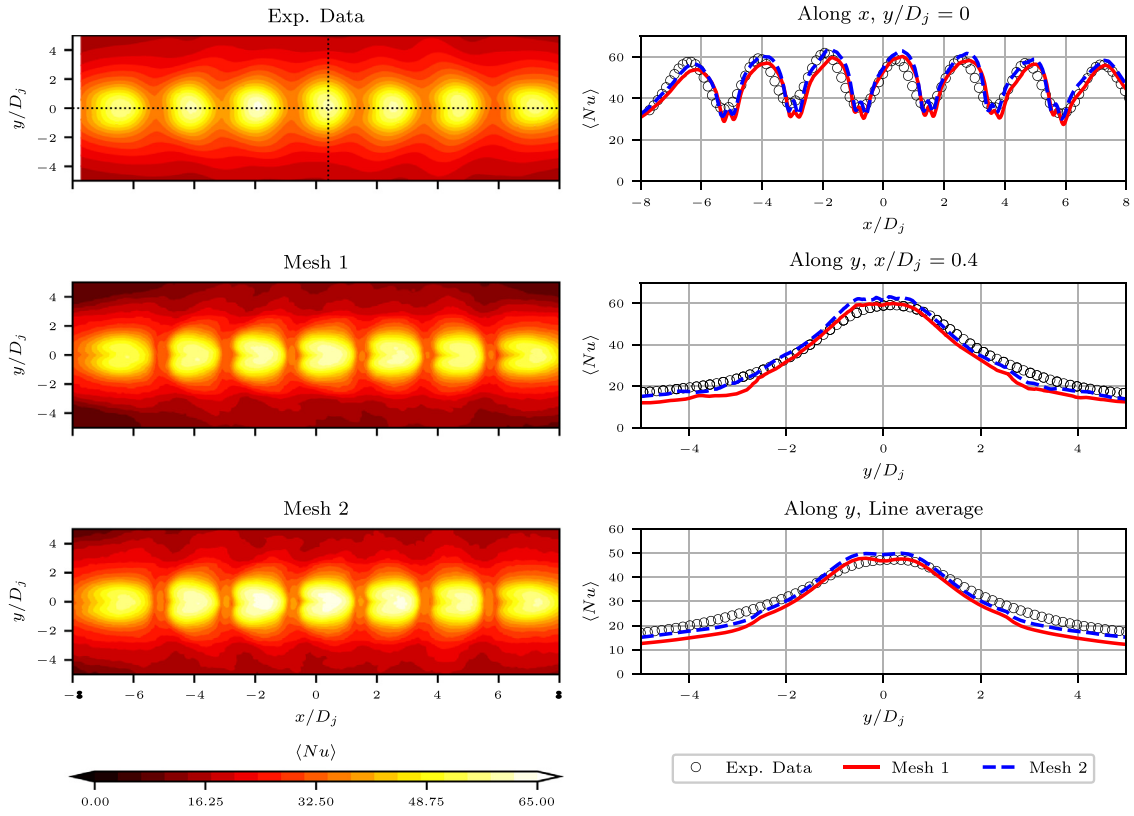

Fig. 15. Comparison of the Nusselt number for the two meshes, for Case 2, $Ma_j =\approx 0.08$. The dotted lines in hte upper left contour represent the locations of the cuts for the profiles along x and y.

be averaged, also shows similarly good agreement with the experimental data. Integrating the line-averaged data from $-4 \leq y/D_j \leq 4$ produces a spatially averaged Nusselt number across the plate of 32.42 for the experimental data, along with 30.32 (6.48% error) for Mesh 1, and 32.20 (0.679% error) for Mesh 2. When taking into account the experimental uncertainty of $6-12\%$ reported by Ahmimache et al. [37], the precision of the LBM-LES data in this current study can be considered excellent.

As in the case for the velocity profiles, the heat transfer plots for Case 2 can be found in Appendix A.1, in Fig. 15. The agreement between the experiments and the LBM-LES solutions is good for this case as well. Regarding the space averaged Nusselt number, the experimental data yields a value of 33.46, with 30.36 (9.26% error) for Mesh 1, and 32.56 (2.69% error) for Mesh 2. Although the error is slightly higher than for Case 1, the results are still in very close agreement.

4.3. Compressibility effects on the nusselt number

As previously discussed in Section 1, compressibility effects on multi impinging jet heat transfer are not universally characterized in the literature, with the experiments of Goodro et al. [39–41] indicating increased heat transfer with higher Mach number, and the RANS study of Ben Ahmed et al. [42] indicating reduced heat transfer. Regarding single jet heat transfer, the experimental study of Fénot et al. (2019) [66] found a modest increase in heat transfer with increasing Mach number near the stagnation point for an impingement distance $H/D_j = 1$. By contrast, for an impingement distance of $H/D_j = 5$, they reported essentially no effect of the Mach number on the stagnation point heat transfer. The DNS of Wilke and Sesterhenn [67] and the LES of Otero-Pérez and Sandberg [62] report a positive impact near the stagnation point, provided that $\lambda_{ref} = \lambda(T = T_j)$ is used in the calculation of the Nusselt number [62]. The compressibility effects of the Mach number in the stagnation region are summarized in Table 3.

Fig. 11 shows the Mach number effects on the wall heat transfer for Case 1, using Mesh 2. $T_{ref} = T_{aw}$ is used to calculate h, and $\lambda_{ref} = \lambda(T = T_j)$ is used to calculate the Nusselt number. The Mach number is positively correlated with the heat transfer at the stagnation point. By contrast, further downsteam from the stagnation points, for $||y/D_j|| > 1.5$, the line-averaged Nusselt number curves are essentially identical, and thus independent of the Mach number. The behavior of these curves is qualitatively very similar to the results of Otero-Pérez et al. [62] for $\lambda_{ref} = \lambda(T = T_j)$ (denoted as Nu^* in their manuscript).

Because the original test case involves a flow at $Ma_j \approx 0.08$, it can be tempting to use PGS in order to accelerate the calculation and achieve faster convergence. This practice has been used by finite volume compressible solvers in order to avoid the excessively short time steps imposed by the acoustic CFL number [68]. In the present study, the $Ma_j \approx 0.30$ case required 1/3 the amount of CPU time as the test case corresponding to $Ma_j \approx 0.08$ (corresponding to the reference data of Ahmimache (2022) [37]), and produced Nusselt number profiles that varied only modestly compared to the true configuration if the adiabatic wall temperature was used as a normalization.

Fig. 12 shows the Nusselt number distribution depending on the value of T_{ref} used to calculate h, with the choice being either the adiabatic wall temperature T_{aw} or the pipe injection temperature T_p. For $Ma_j \approx 0.08$, the profiles are unchanged, as the compressibility effects are so weak that $T_{aw} \approx T_j$. By contrast, even for the modest Mach number of 0.30, the adiabatic wall temperature profile is sufficiently modified and non-homogeneous so as to produce qualitatively different results. The maximal heat transfer is located not at the stagnation points, but adjacent to them. This is because the stagnation point experiences additional heating due to com-

Table 3
Summary of the effects of the Mach number on stagnation region heat transfer found in the literature and in the present study.

Study	Configuration	H/D_j	T_{ref}	λ_{ref}	Result
Present (LES)	Multi-jet	3	T_{aw}	$\lambda(T = T_j)$	Positive correlation
Goodro et al. [40] (Exp.)	Multi-jet	3	T_t	N/S	Positive correlation
Ben Ahmed et al. [42] (RANS)	Multi-jet	9	T_t	N/S	Negative correlation
Fénot et al. (2019) [66] (Exp.)	Single jet	1, 5	T_{aw}	$\lambda(T = T_{aw})$	Positive correlation ($H/D = 1$), no impact ($H/D = 5$)
Wilke and Sesterhenn [67]. (DNS)	Single jet	5	T_t	λ_{const} [62]	Positive correlation
Otero-Pérez and Sandberg [62]. (LES)	Single jet	4.5	T_{aw}	$\lambda(T = T_j)$	Positive correlation if $\lambda_{ref} = \lambda(T = T_j)$

pressible phenomena, increasing the value of T_w and hence reducing Nu. The rise in temperature due to compressibility effects then decays further away from the stagnation point [62]. Furthermore, the present multi-jet configuration, which involves the rapid acceleration of flow from a large pipe into small orifices, leads to a non-negligible drop in static temperature in the free jets at $Ma \approx 0.3$ and $Ma \approx 0.5$, a phenomenon observed by Oliver et al. [69].

When an additional, preliminary simulation is performed to recover T_{aw}, the aforementioned phenomena are taken into account and the location of maximal heat transfer is returned to the stagnation points. Thus, the additional simulation for T_{aw} is superfluous for the $Ma_j \approx 0.08$ test case, but not for the $Ma_j \approx 0.30$ one. For PGS approaches, the reduced CPU time per convective time comes at the cost of performing an additional simulation, due to the emergence of a temperature drop in the orifices as well as non-homogeneous adiabatic wall temperature variation due to pressure work at the walls. These phenomena are not negligible at $Ma_j \approx 0.3$, rendering the PGS approach less attractive, although it is possible that a PGS approach at $Ma_j \approx 0.2$ may be a good compromise between reducing simulation time and avoiding the introduction of noticeable compressible phenomena.

5. Conclusion

An LES of a multi-impinging thermal jet test case consisting of a single row of seven jets emerging from a perforated pipe was performed under a variety of conditions using a compressible Lattice Boltzmann solver. A strong and weak cross flow test case were tested. The Mach number was also varied, using a Pressure Gradient Scaling approach. The strong upstream crossflow condition required the use of a dynamic mass flow condition, which successfully reproduced the correct distribution of fluid flow. The flow statistics and heat transfer fields of the low Mach test cases were then validated against a rich base of data from a corresponding experiment.

The flow statistics showed good agreement with the experimental data for both test cases, although some discrepancies were found, particularly in the shear layers. This was attributed to the difficulties in adequately capturing the breakdown of laminar shear layers at the modest Reynolds number involved. Better results were found with mesh refinement. The practical difficulties in targeted mesh refinement in the free jet region were highlighted, as the jet exhibits strong three dimensional behavior.

The heat transfer profiles at the heated plate showed excellent agreement, for both test cases. The profiles along x and along y showed relatively little discrepancy with the experimental data. The differences between the simulations and the experiments for the spatially averaged Nusselt number values were small. The simulations produced small secondary peaks which were not seen in the experiment. These were attributed to the formation of very small vortical structures resulting from near-wall flow separation, which may have been too small to detect in the corresponding experimental measurements.

The effect of the Mach number on the wall heat transfer distribution was evaluated. Three Mach numbers were tested, $Ma_j \approx 0.08, 0.30, 0.50$, using the adiabatic wall temperature to calculate the Nusselt number in each case. It was found that an increase in Mach number produced an increase in heat transfer near the stagnation point. Furthermore, the advantages of using pressure gradient scaling in order to reduce the computational time were evaluated. For scaling to $Ma_j \approx 0.3$, it was found that using the pressure gradient scaling approach necessitates an additional simulation to retrieve a qualitatively similar Nusselt number profile to the reference (incompressible) simulation. This significantly reduces the gain in computational time.

Data availability

The data that support the findings of this study are available from the corresponding author upon reasonable request.

Declaration of Competing Interest

The authors declare that they have no known competing financial interests or personal relationships that could have appeared to influence the work reported in this paper.

CRediT authorship contribution statement

Minh Nguyen: Conceptualization, Software, Validation, Investigation, Writing – original draft. **Jean-François Boussuge:** Conceptualization, Supervision, Writing – review & editing. **Pierre Sagaut:** Conceptualization, Supervision, Writing – review & editing. **Juan-Carlos Larroya-Huguet:** Conceptualization, Supervision, Writing – review & editing.

Acknowledgements

The authors would like to thank Yassine Ahmimache and Arthur Colombié for their insightful advice. Acknowledgments are also expressed to Safran Aircraft Engines and ANRT/CIFRE convention No. 2019/1220 for their financial support, as well as for access to high performance computing resources. This work has been carried out using ProLB, a lattice-Boltzmann solver currently being developed by a consortium including CS Group, Airbus, Renault, Aix-Marseille Université, and École Centrale Lyon.

Appendix A.

A1. Flow field and heat transfer for case 2

References

[1] J.W. Baughn, S. Shimizu, Heat transfer measurements from a surface with uniform heat flux and an impinging jet, J. Heat Transf. 111 (4) (1989) 1096–1098, doi:10.1115/1.3250776.

[2] M. Fenot, J.-J. Vullierme, E. Dorignac, Local heat transfer due to several configurations of circular air jets impinging on a flat plate with and without semi-confinement, Int. J. Therm. Sci. 44 (2005) 665–675, doi:10.1016/j.ijthermalsci.2004.12.002.

[3] M. Tummers, J. Jacobse, J. Voorbrood, Turbulent flow in the near field of a round impinging jet, Int. J. Heat Mass Transf 54 (23–24) (2011) 4939–4948, doi:10.1016/j.ijheatmasstransfer.2011.07.007.

[4] P. Grenson, O. Léon, P. Reulet, B. Aupoix, Investigation of an impinging heated jet for a small nozzle-to-plate distance and high reynolds number: an extensive experimental approach, Int. J. Heat Mass Transf 102 (2016) 801–815, doi:10.1016/j.ijheatmasstransfer.2016.06.076.

[5] H. Yadav, A. Agrawal, Effect of vortical structures on velocity and turbulent fields in the near region of an impinging turbulent jet, Phys. Fluids 30 (035107) (2018), doi:10.1063/1.5001161.

[6] M. Hadžiabdić, K. Hanjalić, Vortical structures and heat transfer in a round impinging jet, J. Fluid Mech. 596 (2008) 221–260, doi:10.1017/S002211200700955X.

[7] N. Uddin, S. Neumann, B. Weigand, LES Simulations of an impinging jet: on the origin of the second peak in the nusselt number distribution, Int. J. Heat Mass Transf 57 (1) (2013) 356–368, doi:10.1016/j.ijheatmasstransfer.2012.10.052.

[8] T. Dairay, V. Fortuné, E. Lamballais, L.-E. Brizzi, Direct numerical simulation of a turbulent jet impinging on a heated wall, J. Fluid Mech. 764 (2015) 362–394, doi:10.1017/jfm.2014.715.

[9] P. Aillaud, F. Duchaine, L.Y.M. Gicquel, S. Didorally, Secondary peak in the nusselt number distribution of impinging jet flows: a phenomenological analysis, Phys. Fluids 28 (2016) 606–619, doi:10.1063/1.4963687.

[10] P. Grenson, H. Deniau, Large-eddy simualtion of an impinging heated jet for a small nozzle-to-plate distance and high reynolds number, Int. J. Heat Fluid Flow 68 (2017) 348–363, doi:10.1016/j.ijheatfluidflow.2017.09.014.

[11] A. Colombie, E. Laroche, F. Chedevergne, R. Manceau, F. Duchaine, L. Gicquel, Large-eddy-simulation-based analysis of reynolds-stress budgets for a round impinging jet, Phys. Fluid. 33 (11) (2021) 511–525, doi:10.1063/5.0064009.

[12] K. Jambunathan, E. Lai, M. Moss, B. Button, A review of heat transfer data for single circular jet impingement, Int. J. Heat Fluid Flow 13 (2) (1992) 106–115, doi:10.1016/0142-727X(92)90017-4.

[13] N. Zuckerman, N. Lior, Jet impingement heat transfer: physics, correlations, and numerical modeling, Adv. Heat Transfer 39 (2006) 565–631, doi:10.1016/S0065-2717(06)39006-5.

[14] G.M. Carlomagno, A. Ianiro, Thermo-fluid-dynamics of submerged jets impinging at short nozzle-to-plate distance: a review, Exp. Therm Fluid Sci. 58 (2014) 15–35, doi:10.1016/j.expthermflusci.2014.06.010.

[15] R. Viskanta, Heat transfer to impinging isothermal gas and flame jets, Exp. Therm Fluid Sci. 6 (1993) 111–134.

[16] M. Draksler, B. Končar, L. Cizelj, B. Nićeno, Large eddy simulation of multiple impinging jets in hexagonal configuration - flow dynamics and heat transfer characteristics, Exp. Therm. Fluid Sci. 109 (2017) 16–27.

[17] L. Geers, M. Tummers, K. Hanjalić, Wall imprint of turbulent structures and heat transfer in multiple impinging jet arrays, Exp. Fluids 36 (2004) 946–958, doi:10.1007/s00348-004-0778-2.

[18] L. Geers, K. Hanjalić, M. Tummers, Wall imprint of turbulent structures and heat transfer in multiple impinging jet arrays, J. Fluid Mech. 546 (2006) 255–284, doi:10.1017/S002211200500710X.

[19] B. Weigand, S. Spring, Multiple jet impingement - a review, Heat Transf. Res. 42 (2) (2011) 101–142, doi:10.1615/HeatTransRes.v42.i2.30.

[20] E. Laroche, M. Fénot, E. Dorignac, J.J. Vuillerme, L.E. Brizzi, J.C. Larroya, A combined experimental and numerical investigation of the flow and heat transfer inside a turbine vane cooled by jet impingement, J. Turbomach. 140 (3) (2018), doi:10.1115/1.4038411.

[21] R.D. Soghe, L. Mazzei, L. Tarchi, L. Cocchi, A. Picchi, B. Facchini, L. Descamps, J. Girardeau, M. Simon, Development of experimental and numerical methods for the analysis of active clearance control systems, J. Eng. Gas Turbine Power 143 (2) (2021), doi:10.1115/1.4049354.

[22] J. Hossain, E. Fernandez, C. Garrett, J. Kapat, Flow and heat transfer analysis in a single row narrow impingement channel: Comparison of piv, les, and rans to identify rans limitations, Turbo Expo: Power for Land, Sea, and Air, volume 50879, American Society of Mechanical Engineers, 2017, doi:10.1115/GT2017-63994. V05AT16A009

[23] J.J. Otero-Pérez, R.D. Sandberg, S. Mizukami, K. Tanimoto, High-fidelity simulations of multi-jet impingement cooling flows, J. Turbomach. 143 (2021) 081011, doi:10.1115/1.4050446.

[24] Y. Ahmimache, Caractérisation expérimentale et numérique des transferts thermiques par impact de jets - faible nombre de Reynolds : application au refroidissement du carter de turbine basse pression dun turboréacteur, Université de Poitiers, 2022 Ph.D. thesis.

[25] S. Marié, D. Ricot, P. Sagaut, Comparison between lattice boltzmann method and navier-stokes high order schemes for computational aeroacoustics, J. Comput. Phys. 228 (2009) 1056–1070.

[26] A. Xu, L. Shi, T.S. Zhao, Accelerated lattice boltzmann simulation using gpu and openacc with data management, Int. J. Heat Mass Transf. 109 (2017) 577–588, doi:10.1016/j.ijheatmasstransfer.2017.02.032.

[27] A. Xu, B.T. Li, Multi-gpu thermal lattice boltzmann simulations using openacc and mpi, Int. J. Heat Mass Transf. 201 (2023) 123649, doi:10.1016/j.ijheatmasstransfer.2022.123649.

[28] Y. Hou, D. Angland, A. Sengissen, A. Scotto, Lattice-Boltzmann and Navier-Stokes simulations of the partially dressed, cavity-closed nose landing gear benchmark case, in: 25th AIAA/CEAS Aeroacoustics Conference, 2019, pp. 1–20, doi:10.2514/6.2019-2555.

[29] Y. Feng, P. Bovin, J. Jacob, P. Sagaut, Hybrid recursive regularized thermal lattice boltzmann model for high subsonic compressible flows, J. Comput. Phys. 394 (2019) 82–99, doi:10.1016/j.jcp2019.05.031.

[30] S. Guo, Y. Feng, J. Jacob, F. Renard, P. Sagaut, An efficient lattice boltzmann method for compressible aerodynamics on d3q19 lattice, J. Comput. Phys. 418 (2020) 109570, doi:10.1016/j.jcp.2020.109570.

[31] G. Farag, S. Zhao, T. Coratger, P. Boivin, G. Chiavassa, P. Sagaut, A pressure-based regularized lattice-boltzmann method for the simulation of compressible flows, Phys. Fluid. 32 (2020) 066106, doi:10.1063/5.0011839.

[32] S. Guo, Y. Feng, P. Sagaut, Improved standard thermal lattice boltzmann model with hybrid recursive regularization for commpressible laminar and turbulent flows, Phys. Fluids 32 (2020) 126108, doi:10.1063/5.0033364.

[33] F. Renard, Y. Feng, J.F. Boussuge, P. Sagaut, Improved compressible hybrid lattice boltzmann method on standard lattice for subsonic and supersonic flows, Comput. Fluid. 219 (2021) 104867, doi:10.1016/j.compfluid.2021.104867.

[34] G. Farag, T. Coratger, G. Wissocq, S. Zhao, P. Boivin, P. Sagaut, A unified hybrid lattice-boltzmann method for compressible flows: bridging between pressure-based and density-based methods, Phys. Fluid. 33 (2021) 086101, doi:10.1063/5.0057407.

[35] T. Coratger, G. Farg, S. Zhao, P. Boivin, P. Sagaut, Large-eddy lattice-boltzmann modeling of transonic flows, Phys. Fluid. 33 (2021) 115112, doi:10.1063/5.0064944.

[36] M. Nguyen, J.F. Boussuge, P. Sagaut, J.C. Larroya-Huguet, Large eddy simulation of a thermal impinging jet using the lattice boltzmann method, Phys. Fluid. 34 (2022) 055115, doi:10.1063/5.0088410.

[37] Y. Ahmimache, M. Fénot, F. Plourde, L. Descamps, Heat transfer and flow velocity study of a row of jets emerging from a perforated pipe at a low reynolds number, Int. J. Heat Mass Transf. 183 (2022) 122067, doi:10.1016/j.ijheatmasstransfer.2021.122067.

[38] L. Cocchi, A. Picchi, B. Facchini, R.D. Soghe, L. Mazzei, L. Tarchi, L. Descamps, M. Rotenberg, Effect of jet-to-jet distance and pipe position on flow and heat transfer features of active clearance control systems, Turbo Expo: Power for Land, Sea, and Air, volume 84980, American Society of Mechanical Engineers, 2021, doi:10.1115/GT2021-59158. V05BT14A007

[39] M. Goodro, J. Park, P. Ligrani, M. Fox, H.K. Moon, Effects of mach number and reynolds number on jet array impingement heat transfer, Int. J. Heat Mass Transf. 50 (1–2) (2007) 367–380, doi:10.1016/j.ijheatmasstransfer.2006.06.007.

[40] M. Goodro, J. Park, P. Ligrani, M. Fox, H.K. Moon, Effects of hole spacing on spatially-resolved jet array impingement heat transfer, Int. J. Heat Mass Transf. 51 (25–26) (2008) 6243–6253, doi:10.1016/j.ijheatmasstransfer.2008.05.004.

[41] M. Goodro, P. Ligrani, M. Fox, H.K. Moon, Mach number, reynolds number, jet spacing variations: full array of impinging jets, J. Thermophys. Heat Transf. 24 (1) (2010) 133–144, doi:10.2514/1.44029.

[42] F.B. Ahmed, B. Weigand, K. Meier, Heat transfer and pressure drop characteristics for a turbine casing impingement cooling system, in: International Heat Transfer Conference, volume 49408, 2010, pp. 199–212, doi:10.1115/IHTC14-22817.

[43] J.D. Ramshaw, P.J. O'Rourke, L.R. Stein, Pressure gradient scaling method for fluid flow with nearly uniform pressure, J. Comput. Phys. 58 (3) (1985) 361–376, doi:10.1016/0021-9991(85)90168-8.

[44] CS Systémes - ProLB, (http://www.prolb-cfd.com/), Accessed: 2022-07-26.

[45] M. Bauer, G. Silva, U. Rüde, Letter to the editor: truncation errors of the d3q19 lattice model for the lattice boltzmann method, J. Comput. Phys. 405 (2020), doi:10.1016/j.jcp.2019.109111.

[46] J. Jacob, O. Malaspinas, P. Sagaut, A new hybrid recursive regularised bhatnagar-gross-krook collision model for lattice boltzmann method-based large eddy simulation, J. Turbul. 19 (11–12) (2018) 1051–1076, doi:10.1080/14685248.2018.1540879.

[47] T. Astoul, G. Wissocq, J.-F. Boussuge, A. Sengissen, P. Sagaut, Lattice boltzmann method for computational aeroacoustics on non-uniform meshes: a direct grid coupling approach, J. Comput. Phys. 447 (2021) 110667, doi:10.1016/j.jcp.2021.110667.

[48] E. Lévêque, F. Toschi, L. Shao, Shear-improved smagorinsky model for large-eddy simulation of wall-bounded turbulent flows, J. Fluid Mech. 570 (2007) 491–502, doi:10.1017/S0022112006003429.

[49] T.J. Poinsot, S.K. Lele, Boundary conditions for direct simulations of compressible viscous flows, J. Comput. Phys. 101 (1) (1992) 104–129, doi:10.1016/0021-9991(92)90046-2.

[50] Y. Feng, S. Guo, J. Jacob, P. Sagaut, Solid wall and open boundary conditions in hybrid recursive regularized lattice boltzmann method for compressible flows, Phys. Fluid. 31 (2019) 126103, doi:10.1063/1.5129138.

[51] G. Lodato, L. Vervisch, P. Domingo, Three-dimensional boundary conditions for direct and large-eddy simulation of compressible viscous flows, J. Comput. Phys. 227 (10) (2008) 5105–5143, doi:10.1016/j.jcp.2008.01.038.

[52] G. Lodato, L. Vervisch, P. Domingo, A compressible wall-adapting similarity mixed model for large-eddy simulation of the impinging round jet, Phys. Fluid. 21 (3) (2009) 035102, doi:10.1063/1.3068761.

[53] N. Odier, T. Poinsot, F. Duchaine, L. Gicquel, S. Moreau, Inlet and outlet characteristics boundary conditions for large eddy simulations of turbomachinery, Turbo Expo: Power for Land, Sea, and Air, volume 58578, American Society of Mechanical Engineers, 2019, doi:10.1115/GT2019-90747. V02CT41A020

[54] G.E. Khoury, P. Schlatter, A. Noorani, P.F. Fischer, G. Brethouwer, A.V. Johansson, Direct numerical simulation of turbulent pipe flow at moderately high reynolds numbers, Flow Turbul. Combust. 91 (3) (2013) 475–495.

[55] W. Béchara, C. Bailly, P. Lafon, S. Candel, Stochastic approach to noise modeling for free turbulent flows, AIAA J. 32 (3) (1994) 455–463, doi:10.2514/3.12008.

[56] C. Bailly, D. Juvé, A stochastic approach to compute subsonic noise using linearized euler's equations, in: 5th AIAA CEAS Aeroacoustics Conference Exhibition, 1999, pp. 496–506, doi:10.2514/6.1999-1872.

[57] U. Piomelli, J.R. Chasnov, Large-Eddy Simulations: Theory and Applications, Springer, 1996, doi:10.1007/978-94-015-8666-5_7.
[58] H. Touil, D. Ricot, E. Lévêque, Direct and large-eddy simulation of turbulent flows on composite multi-resolution grids by the lattice boltzmann method, J. Comput. Phys. 256 (2014) 220–233, doi:10.1016/j.jcp.2013.07.037.
[59] B. Dorschner, N. Frapolli, S.S. Chikatamarla, I.V. Karlin, Grid refinement for entropic lattice boltzmann models, Phys. Rev. E 94 (5) (2016) 053311, doi:10.1103/PhysRevE.94.053311.
[60] J. Mi, D.S. Nobes, G.J. Nathan, Influence of jet exit conditions on the passive scalar field of an axisymmetric free jet, J. Fluid Mech. 432 (2001) 91–125, doi:10.1017/S0022112000003384.
[61] M. Fénot, E. Dorignac, Heat transfer and flow structure of an impinging jet with upstream flow, Int. J. Therm. Sci. 109 (2016) 386–400, doi:10.1016/j.ijthermalsci.2016.06.010.
[62] J.J. Otero-Pérez, R.D. Sandberg, Compressibility and variable inertia effects on heat transfer in turbulent impinging jets, J. Fluid Mech. 887 (2020) A15, doi:10.1017/jfm.2020.5.
[63] C. Carcasci, An experimental investigation on air impinging jets using visualisation methods, Int. J. Therm. Sci. 38 (9) (1999) 808–818, doi:10.1016/S1290-0729(99)80036-2.
[64] Y. Ichikawa, M. Motosuke, Y. Kameya, M. Yamamota, S. Honami, Three-dimensional flow characterization of a square array of multiple circular impinging jets using stereoscopic piv and heat transfer relation, J. Visualizat. 19 (1) (2016) 89–101, doi:10.1007/s12650-015-0296-8.
[65] M. Wae-hayee, K. Yeranee, I. Piya, Y. Rao, C. Nuntadusit, Heat transfer correlation of impinging jet array from pipe nozzle under fully developed flow, Appl. Therm. Eng. 154 (2019) 37–45, doi:10.1016/j.applthermaleng.2019.03.044.
[66] M. Fénot, X. Trinh, E. Dorignac, Flow and heat transfer of a compressible impinging jet, Int. J. Therm. Sci. 136 (2019) 357–369, doi:10.1016/j.ijthermalsci.2018.10.035.
[67] R. Wilke, J. Sesterhenn, Statistics of fully turbulent impinging jets, J. Fluid Mech. 764 (2017) 795–824, doi:10.1017/jfm.2017.414.
[68] A. Aniello, D. Schuster, P. Werner, J.F. Boussuge, M. Gatti, C. Mirat, L. Selle, T. Schuller, T. Poinsot, U. Rühde, Comparison of a finite volume and two lattice boltzmann solvers for swirled confined flows, Comput. Fluid. 241 (2022) 105463, doi:10.1016/j.compfluid.2022.105463.
[69] T.A. Oliver, D.G. Bogard, R.D. Moser, Large eddy simulation of compressible, shaped-hole film cooling, Int. J. Heat Mass Transf. 140 (2019) 498–517, doi:10.1016/j.ijheatmasstransfer.2019.04.119.